UNIVERSITY OF TWENTE.

Faculty of Science & Technology,
Biomedical Engineering

Source reconstruction of ANT-DBS induced evoked potentials and epileptiform discharges in patients with refractory epilepsy

Linda Loosveld, BSc

Master thesis
March 2024

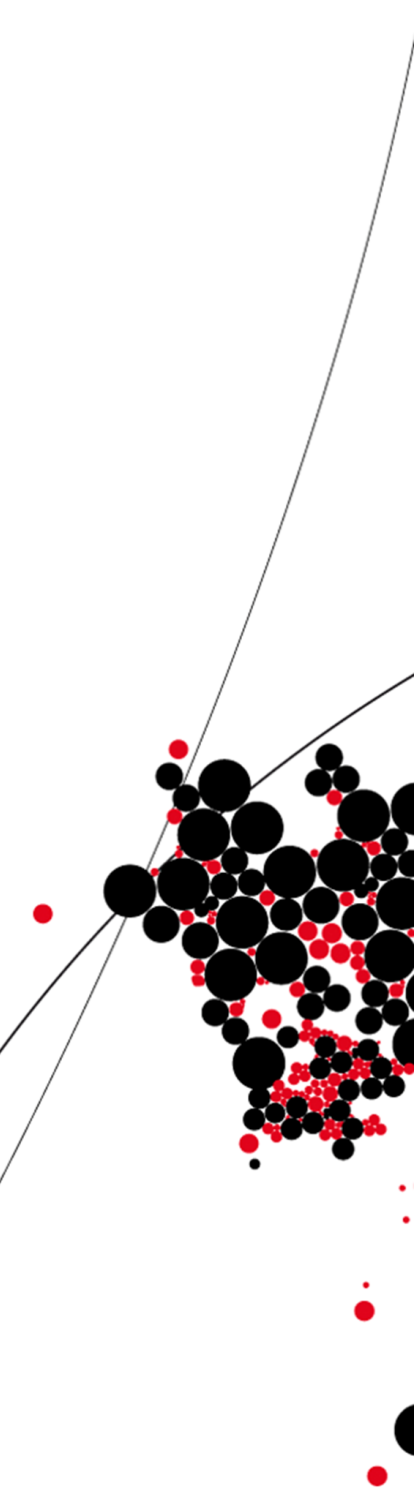

Supervisors:
Dr. rer. nat. M.C. Piastra
Prof. dr. ir. M.J.A.M. van Putten
Dr. ir. B.C. Schwab

Clinical Neurophysiology Group
University of Twente

1 Acknowledgments

Looking back on my master thesis, I am so fortunate to have had the opportunity to work on this assignment. Even though I came across a lot of challenges, I discovered an even stronger passion for neuroscience. The project was filled with setbacks, which made me learn a lot in both a professional and personal level. However, I could never have done this all by myself. Therefore, I would like to acknowledge those who contributed.

First a very special thanks to my daily supervisor, Maria Carla. I genuinely mean it when I express that I couldn't have wished for a better supervisor. You were always filled with enthusiasm and great new ideas, never hesitating to help me solve my problems. You set an exemplary standard, and I've learned so much from you. Besides, Marleen Tjepkema also contributed a lot to this project. Even though you were not officially part of my committee, you were always willing to think along and showed lots of enthusiasm for this project. You also made sure I had all the data I needed to get to the results. I enjoyed all the useful and fun cookie meetings. I'm also very grateful for Michel van Putten and Bettina Schwab, my other committee members who took the time and effort to read the report and listen to my presentations, always indulging me with lots of useful feedback.

I also want to show some appreciation for the CNPH group in general. I had a great time while working on my research, filled with fully packed tables, fun talks, activities, and monthly drinks. I hope we will stay in touch!

2 List of abbreviations

- ANT = Anterior nucleus of the thalamus
- BEM = Boundary Element Method
- CSF = Cerebrospinal fluid
- ED = Epileptiform discharge
- EP = Evoked potential
- FEM = Finite Element Method
- FFT = Fast Fourier transform
- GTC = Generalized tonic-clonic
- ICA = Independent Component Analysis
- MN = Minimum norm
- MTT = Mammillothalamic tract
- RE = Relative error
- RV = Residual variance
- SF = Scaling factor
- STN = Subthalamic nucleus

Abstract

Introduction: Epilepsy is a chronic neurological disorder characterized by recurrent seizures which is primarily treated with medication. However, 30% to 40% of the patients are refractory to drug treatment and neuromodulation interventions, such as deep brain stimulation (DBS), have emerged as potential alternatives for these patients. The response rate after 1 year is 43%, the parameter titration is based on trial and error, and the underlying mechanisms are still far from understood. To advance our understanding, in this thesis, we investigated DBS-triggered evoked potentials recorded at the scalp and the personalized overlap in cortical activation maps for the DBS-triggered and epileptic activity.

Methods: We analyzed two EEG datasets of one patient during DBS stimulation to investigate short and long-latency responses and two epileptiform discharges. For the analysis of evoked potentials, we separated even and odd DBS artifacts corresponding to hemisphere-wise stimulation. We reconstructed sources of those evoked potentials and epileptiform discharges, leading to the DBS and epilepsy map. An analysis of the overlap between these two maps is conducted. A comprehensive exploration of EEG data filtering techniques is undertaken to make this possible.

Results: After applying template subtraction with linear interpolation to reduce the DBS artifact from the EEG signal, we found four distinct components of ANT-DBS evoked potentials at 5.5 (5.5), 25 (41), 63 (62) and 157 (180) ms after averaging odd (even) DBS artifacts. The temporal progression of dipoles based on the odd and even peaks exhibited similarities. However, differences in lateralization occurred between stimulation in the two hemispheres. For the even peaks, the sources were localized in the thalamus and cingulate gyrus, which is consistent with the hypothesis of the circuit of Papez being involved after DBS. For the odd peaks, the source analysis resulted in more lateral dipoles, raising considerations about electrode mapping accuracy or spatial resolution limitations in the source reconstruction pipeline. As to the epileptiform discharges, one was more focal, and one more spread. In the case of the more generalized activity, we see a partial overlap between the DBS map and the epileptic map.

Conclusion: For the first time, we show ANT-DBS-evoked potentials recorded at the scalp. Stimulation in one hemisphere showed progression possibly in the circuit of Papez, as we would expect based on literature. At the source level, the evoked potentials partially overlap with one epileptiform discharge. Additional research is crucial to establish robust conclusions regarding DBS and epilepsy map overlaps. However, the insights gained from this research could play a pivotal role in influencing epilepsy treatment strategies, introducing a predictive parameter for assessing the treatment efficacy of ANT-DBS in refractory epileptic patients.

Contents

3 Introduction

3.1 Epilepsy

Epilepsy is a chronic neurological disorder characterized by recurrent seizures[1]. It is one of the most common neurological conditions, with an incidence of approximately 50 new cases per year per 100,000 in the population[2]. In approximately 75% of the patients, epilepsy manifests during childhood, reflecting the heightened susceptibility of the developing brain to seizures. The occurrence of seizures is a major source of stress, injury, and reduced quality of life for those affected by the disorder[1].

From a neurological perspective, a seizure is a paroxysmal alteration of neurological functioning caused by excessive, hypersynchronous discharges of neurons in the brain[2]. Seizures can originate in the cortex or subcortical structures. A seizure provoked by a reversible insult such as fever or hypoglycemia does not fall under the definition of epilepsy because it is a short-lived secondary condition, not a chronic state.

3.1.1 Classification of epilepsy

Seizures are divided into two main categories: generalized and focal seizures[2,3]. The categories are based on the onset region of the epileptic seizure.

Generalized epilepsy
Generalized seizures begin in bilateral distributed neuronal networks[2]. A seizure can begin focally and later generalize. The main subtypes of generalized seizures are absence, generalized tonic–clonic (GTC), myoclonic, and atonic seizures. Absence seizures involve staring with unresponsiveness to external verbal stimuli, sometimes with eye blinking or head nodding. GTC seizures consist of bilateral symmetric convulsive movements (stiffening followed by jerking) of all limbs with impairment of consciousness. Myoclonic seizures consist of sudden, brief movements that are not associated with any obvious disturbance of consciousness. These brief involuntary muscle contractions may affect one or several muscles. Therefore, myoclonic seizures can be generalized or focal. Atonic seizures involve the loss of body tone, often resulting in a head drop or fall.

Focal epilepsy
Focal seizures originate in neuronal networks limited to only one cerebral hemisphere. The clinical manifestation of a focal seizure depends on the area of the cortex involved. For example, a focal seizure arising from the occipital lobe may involve visual phenomena. Different subtypes of focal seizures include simple focal seizures, complex focal seizures and secondary generalized seizures[3]. Simple focal seizures affect only a small part of the brain, resulting in twitching or changes in sensations, such as a taste or smell. Complex focal seizures can make the patient confused or dazed, resulting in an inability to respond to questions or directions for up to a few minutes. Secondary generalized seizures start as a focal seizure in one part of the brain, but then spread to both sides of the brain, resulting in a generalized seizure. When consciousness is impaired, the seizure is classified as dyscognitive, which is often the case with seizures originating in the temporal lobe. Some seizures are preceded by an aura, which is a focal seizure wherein a patient retains awareness and describes motor, sensory, autonomic, or psychological symptoms. An aura precedes a focal dyscognitive or generalized seizure by seconds or minutes and is most often experienced by patients with temporal lobe epilepsy.

3.1.2 Pathophysiology

The pathophysiology of epilepsy and seizures is diverse, accounting for the many different types of seizure disorders[4]. However, one commonality across epilepsy is a disrupted balance between excitatory (via glutamatergic signaling) and inhibitory (via GABAergic signaling) signals at the synaptic level that can result in seizure activity. Early pharmacologic studies demonstrated that $GABA_{\alpha}$-receptor antagonists and glutamate-receptor agonists could elicit seizure activity in normal animals. This E/I imbalance can result from an alteration at many levels of brain function, from genes and subcellular signaling cascades to widespread neuronal circuits[2]. Further studies demonstrated that interictal spikes commonly observed in EEG recordings from epileptic patients are associated with a large depolarization and subsequent initiation of action potentials in individual neurons[4]. The highly organized structure of cortical tissue with its laminar cell layers facilitates the flow of normal neuronal processing, while also providing a structure highly susceptible to abnormal synchronous activity that can lead to seizure generation. In healthy conditions, excitatory synaptic activity is tightly regulated by inhibitory interneurons. However, genetic mutations, cortical lesions, tumors, devel-

opmental malformations, or acute cortical damage due to trauma or stroke disrupt this regulation allowing cortical networks to become hyper-excitable.

Focal epilepsy accounts for approximately 60% of epilepsy patients. The etiology of focal epilepsy is broad. However, trauma-induced epilepsy is becoming a larger issue as medical advances allow patients to survive more severe traumas that would have been fatal in previous generations. Generalized epilepsy, on the other hand, accounting for approximately 40% of the patients, is usually genetic in etiology. Genetic channelopathies, including voltage-gated sodium channels and $GABA_{\alpha}$ receptors, have been identified for many generalized epilepsy types.

The developing brain is particularly prone to seizures for a variety of physiological reasons[2]. Even in the normal developing brain, excitatory synaptic function develops before inhibitory synaptic function, favoring enhanced excitation and seizure generation. In addition, early in life, the neurotransmitter GABA causes excitation rather than inhibition. These observations partly explain why the very young brain is especially susceptible to seizures. However, seizures cause less structural damage in the developing brain than in the adult brain.

3.1.3 Diagnosis

Epilepsy will mostly be diagnosed based on a neurological examination which assesses focal signs that might implicate or localize cerebral pathology[2]. An important addition to this neurological assessment is an EEG. An EEG measures the potentials on the surface of the scalp, making it possible to detect abnormal electrical activity present usually in between seizures. Those electrical events in between seizures are called epileptiform discharges and can consist of focal spikes or waves occurring in focal epilepsy, or diffuse bilateral spike waves occurring in generalized epilepsy. A routine EEG will, preferably, include wakefulness, drowsiness, and sleep because the prevalence of epileptiform abnormalities varies in these different states of consciousness. Hyperventilation and photic stimulation are activation procedures performed during an EEG to increase the yield of epileptic activity.

3.1.4 Treatment

The first-line treatment for epilepsy is medication. However, 30% to 40% of the patients have seizures that are refractory to treatment with anti-epileptic medication[5]. Surgical resection or ablation can result in seizure reduction in patients. However, not all patients with epilepsy are candidates for those treatments. Furthermore, despite careful selection, some patients may continue to experience seizures post-operatively. In those patients whose seizures are inadequately controlled with medication and surgery, neuromodulation-based interventions, such as deep brain stimulation could be considered[6].

3.2 Deep brain stimulation in epileptic patients

Deep brain stimulation (DBS) involves the implantation of stimulating electrodes in a precisely guided fashion into subcortical structures and, at a later stage, chronic stimulation of these structures. During deep brain stimulation, an electrical current is generated by an implanted pulse generator and delivered directly to the brain via intracranial electrodes[7]. These electrodes are surgically implanted, penetrating deep into the brain tissue using depth electrodes. Electrical current is conducted either between one electrode and the pulse generator (monopolar), between two electrodes (bipolar), or between several electrode contacts (multipolar). The shape of the stimulus current is defined by several parameters, including current amplitude, pulse width, burst duration, and frequency. Initial stimulation settings are generally common to all patients and are adjusted empirically in a trial-and-error fashion until an acceptable response is achieved. The response rate after 1 year is 43% in epileptic patients[8].

Several critical aspects of therapy remain unsolved, in particular how, where and when stimulation should be delivered according to individual anatomical and pathophysiological differences[9]. Clarification of these aspects is difficult as the mechanism of action of DBS is still generally questioned[6]. However, possible mechanisms of DBS include activation of axons, local inhibition, effects on astrocytes, and disturbance of network oscillations[10]. Disruption or modulation of epileptogenic networks most likely plays an important role in the therapeutic effect of DBS on epilepsy. Clinical efficacy has been associated with multiple DBS targets that belong to different anatomical circuits: motor, limbic and memory. This suggests the possibility of a common functional neural network responsible for the anti-seizure effect associated with stimulation in epilepsy. DBS of the anterior nucleus of the thalamus (ANT) has been approved for the treatment of refractory epilepsy[9].

3.2.1 Anterior nucleus of the thalamus

The anterior thalamic nucleus is a vital node within the hippocampal-diencephalic-cingulate circuit that supports spatial learning and memory[11]. The anterior thalamic nucleus is located anteriorly to the thalamus and is composed of the anteromedial, anteroventral, and anterodorsal nuclei, see Figure 1. Although there is much overlap in terms of connections, those nuclei have their own functional specializations.

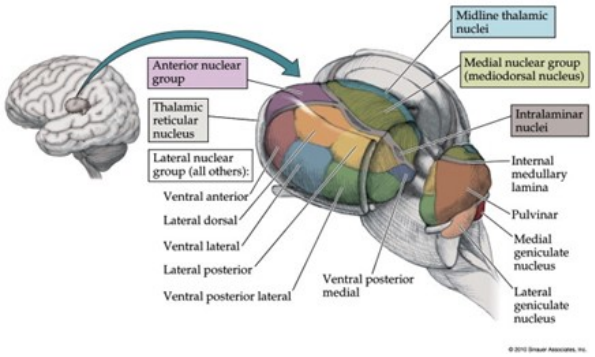

Figure 1: Anatomy of the thalamus. The ANT is visible in pink at the anterior side of the thalamus.

Our understanding of the cognitive functions of the anterior thalamic nuclei has largely been framed by their connectivity within the circuit of Papez. The Papez circuit is believed to control spatial memory and emotions and is composed of the cingulate cortex, entorhinal cortex, parahippocampal gyrus, hippocampus, hypothalamus, and thalamus. The Papez circuit is composed of two parallel loops generated mainly by the cingulum bundle and fornix, see Figure 2[12]. The cingulum bundle is the longest limbic pathway of the Papez circuit generating a large loop connecting the prefrontal projections of the cingulate gyrus to the hippocampus in the parahippocampal gyrus of the temporal lobe. The hippocampus then connects to the mammillary bodies via the fornix. The mammillary bodies project to the ventral thalamus via the mammillothalamic tract (MTT). The ventral thalamus links back into the anterior cingulate gyrus via the thalamic-cingulate projections to complete the Papez circuit. Furthermore, a consideration of anterior thalamic interconnectivity with sites beyond the Papez circuit also points to the potential involvement of these thalamic nuclei in different cognitive functions[11]. For example, the anterior thalamic nuclei are densely interconnected with the frontal cortex. The functional importance of these non-hippocampal connections is, however, poorly understood.

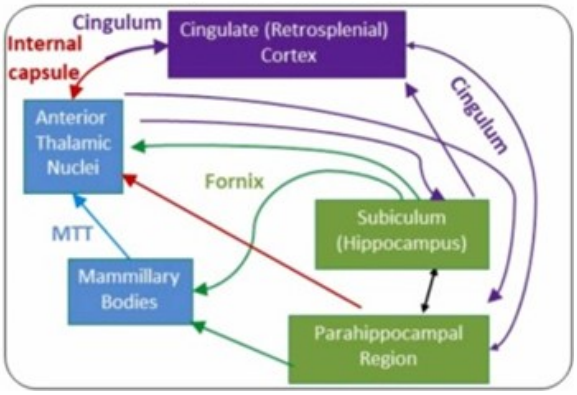

Figure 2: A graphical overview of the circuit of Papez, in which the ANT plays an important role[13]. The two parallel main loops are visible and consist mainly of the cingulum bundle and the fornix.

3.2.2 Stimulation parameters

Stimulation parameters have thus far been selected empirically on the basis of investigators' experience and previous studies such as the SANTE trial. This study investigates the safety of ANT stimulation in patients with drug-resistant epilepsy.[8]. The effects of frequency, voltage, current, pulse width, unilateral versus bilateral stimulation, and cycling versus continuous stimulation on the efficacy are poorly understood[9]. In general, it is thought that low-frequency stimulation increases seizure risk by lowering the seizure threshold and enhancing epileptogenic discharges, whereas higher frequencies desynchronize electrical activity and reduce seizure risk. Common stimulation parameters are $\geq$100 Hz at 1-10 V for ANT stimulation. Most significantly, descriptive analysis of stimulation parameters used during the long-term follow-up of the SANTE cohort found no favorable parameters in frequency, voltage, or pulse width[8]. There were no differences between cycling and continuous stimulation, and no association between output voltage and seizure reduction. Comparison of unilateral to bilateral stimulation also yielded conflicting results. On the other hand, exact positioning of DBS electrodes appears significant as ANT-DBS electrodes located anteriorly, or in the antero-ventral subdivision of the ANT were correlated with a better outcome.

3.2.3 DBS and EEG

EEG measurements can be used to monitor changes in the epileptic manifestations, due to DBS stimulation as well as gaining knowledge about the working mechanism of DBS. However, combining DBS and EEG leads to notable challenges. DBS consists of a train of narrow pulses, with an amplitude greater than 1V[14]. This signal is volume-conducted to the scalp, where it produces large artifacts relative to the scale of neural activity measured using typical electroencephalographic recording devices. Even though stimulation occurs at one specific frequency, these artifacts affect the entire frequency spectrum, including many physiologically relevant frequency bands. The original signal of DBS pulses is a spike train in the time domain, i.e., a square wave containing odd frequency harmonics, not a sinusoidal signal as the EEG signal. In theory, an extremely high (infinite) sampling rate is thus required to ensure a faithful recording of the DBS signal. In practice, DBS pulses are regularly missed or badly captured by the A/D converter which is limited in its acquisition frequency and amplitude range. The probability that a DBS pulse is missed or distorted during recording depends on several factors including the sampling frequency, the type of A/D converter, the DBS frequency, the DBS pulse width and the phase between the DBS signal and the sampling function, the desynchronization between the internal clocks of the stimulation and the recording devices. These measurement errors have their own period, leading to artifactual values outside the range of the actual DBS frequency, the so-called aliasing effect. Moreover, even if the sampling rate is sufficiently high to measure each of the successive peaks in the signal, the jitter between the clocks of the recording and the stimulation devices is further responsible for a non-negligible part of the aliasing effect.

3.2.4 Filtering of the DBS artifact

The occurrence of the DBS artifact results in many artifact removal methods. Simple filtering methods such as oversampling, antialiasing analog filtering, and digital low-pass filtering are not sufficient to remove the DBS artifact. More complex filtering methods that exist for filtering DBS artifacts are neither easy to use nor fully effective at removing the artifacts. In this chapter, we will discuss potential artifact removal methods: template subtraction, Hampel filtering, and independent component analysis.

Template subtraction

Template subtraction is a possible technique for the removal of the DBS artifact[15]. This method makes use of linear interpolation between the onset of stimulation and the start of the passive charge recovery phase, see Figure 3. For the second part of the signal, it subtracts an artifact template from the EEG signal, resulting in a physiological leftover EEG signal. Some forms of artifacts have predefined templates, such as eyeblinks. This is not the case for DBS artifacts, making it necessary to create a scaled template based on the EEG data. Peeters et al. suggest using the signal from the mastoid electrodes, which are assumed not to represent any brain activity but only artifact signals. The relative error between the template and the EEG signal is computed as follows,

$$RE = \frac{template\ \ signal - EEG\ \ signal}{template\ \ signal},$$

where RE are the relative errors. Based on the relative errors, the template is scaled with a scaling factor. This scaling factor is calculated as follows,

$$SF = 1 - mean(RE).$$

In this equation, SF equals the scaling factor. This scaling factor is multiplied with the template to create a scaled template. The scaled template is subtracted from the EEG data, leaving presumably only physiological brain activity.

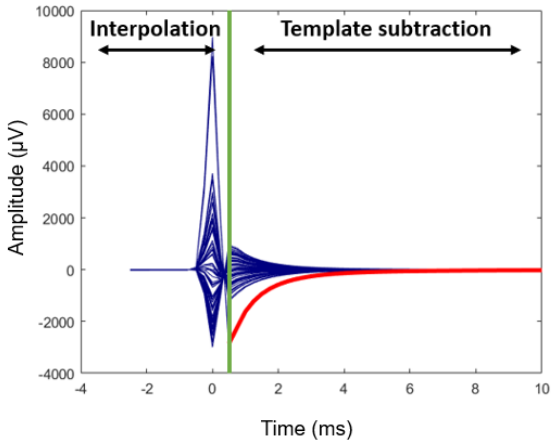

Figure 3: Template subtraction as described by Peeters et al.[15] The method consists of two parts: linear interpolation and template subtraction. The start of the passive charge recovery phase is the division between those two parts, as visualized with a green line. The red line shows the average of the mastoid electrodes, which will be used for template subtraction.

Hampel identifier

The Hampel filter described by Allen et al. is an off-line frequency-domain filtering method for the removal of spectral outliers, based on the median value of the data sequence[16,17]. The median value is more robust than other statistics such as the mean, standard deviation and kurtosis since those are highly influenced by outliers[17]. The filter transforms a time-domain signal into the frequency domain with the fast Fourier transform (FFT), detects outliers in the real and imaginary spectra with the Hampel identifier, replaces those outliers with the local median value, and transforms the cleaned spectra back to the time domain via the inverse FFT[16]. Operating on the complex spectra in such a manner, as opposed to the power spectrum, ensures zero phase distortion at the non-interpolated frequencies, which results in minimum distortion to the reconstructed signal and hence preserves temporal information. The Hampel identifier is a robust statistic that defines data points in a sequence $x_j|j = 1 : N$ as outliers if their absolute difference from the median value $x*$ is greater than a pre-determined threshold t, as given by

$$|x_j - x*| > tS,$$

where S is a scale estimator that quantifies the statistical dispersion of the median's absolute deviation of a data sequence and is analogous to the spread around the mean value described by the standard deviation. S can be calculated as follows,

$$S = 1.4286 * median(|x_j - x*|),$$

where the value 1.4286 is chosen so that the value of S equals the standard deviation of the normal distribution of the data and covers 50% of the standard normal cumulative distribution function. S becomes 0 when more than 50% of the data points have the same value as x_j. The data sequence x_j is formed by a sliding window of length N. There are thus two parameters, t and N, that control the sensitivity of the filter. However, in practice for relatively large N, t can typically be set to approximately 5.

The length of the window L is critical to the operation of the Hampel filter[17]. Outliers are unlikely to be spike-like data points occupying one frequency bin. They are, however, much more likely to be spread over several frequency bins as a result of spectral leakage. It is essential to ensure that the Hampel window is sufficiently long to capture these broader spikes as well as any leakage in adjacent bins. If the window length is too short, outliers will either go undetected or else will be replaced by median values that are influenced by the adjacent leakage. The minimum fraction of the window length at which the median value could be an outlier, is 0.5. This implies that the window length should be at least twice the width of the spectral peak. However, a higher window length also increases the computational cost of the filtering method[18]. In the present work, we adopted a filter window length of ten times the peak width to allow for adjacent spectral leakage. It has been shown that the Hampel identifier is capable of detecting multiple outliers in a data sequence[17].

Independent component analysis

Independent component analysis (ICA) is one of the most well-known algorithms that are used to solve blind source separation problems, in which original signals are extracted from mixtures of signals[19]. A mixture of two sources can be described as,

$$X = \begin{pmatrix} X_1 \\ X_2 \end{pmatrix} = \begin{pmatrix} as_1 + bs_2 \\ cs_1 + ds_2 \end{pmatrix} = \begin{pmatrix} a & b \\ c & d \end{pmatrix} \begin{pmatrix} s_1 \\ s_2 \end{pmatrix} = As,$$

where X are the mixed signals, s are the two sources and A is the mixing matrix. Given two mixture signals X_1 and X_2, the aim is to extract source signals Y_1 and Y_2 which can be achieved by searching for unmixing coefficients α,β,γ and δ:

$$Y_1 = \alpha X_1 + \beta X_2,$$
$$Y_2 = \gamma X_1 + \delta X_2.$$

The unmixing coefficients form weight vectors W_1 and W_2 which create an unmixing matrix $W = \begin{pmatrix} W_1 & W_2 \end{pmatrix}^T$. This unmixing matrix represents the inverse of A. With the unmixing matrix we can calculate the source signal from the mixture signal as follows:

$$X \to Y : Y = W^T X,$$

When applying this to all mixture signals, we find a formula as follows:

$$Y_1 = \alpha X_1 + \beta X_2 = W_1^T X,$$
$$Y_2 = \gamma X_1 + \delta X_2 = W_2^T X.$$

The unmixing process can be achieved by rotating the rows of W. This rotation will continue until each row in W (W_1 or W_2) finds the orientation which is orthogonal to other transformed signals. The source signals are then extracted by projecting a mixture of signals onto that orientation.

In practice, changing the length or orientation of weight vectors has a great influence on the extracted signals. This is the reason why the extracted signals may be not identical to the original source signals. ICA has many algorithms such as FastICA, projection pursuit, and Infomax. The main goal of these algorithms is to extract independent components by the non-Gaussianity, minimizing the mutual information, or using maximum likelihood estimation method. All approaches simply search for a rotation or unmixing matrix W. Projecting the data onto that rotation matrix extracts independent signals.

3.3 Evoked potentials

Evoked potentials (EPs) are electrical responses, often only several microvolts in amplitude, recorded in response to an appropriate stimulus, such as DBS[20]. The potential that is evoked by the stimulus is time-locked to the stimulus in contrast to random spontaneous electrical fluctuations such as electroencephalographic activity or other electrical noise.

Literature about evoked potentials after DBS of the ANT is scarce. However, one research applied 2 Hz DBS in the ANT of five participants resulting in strong EPs at 35 and 38 ms, as well as weak EPs at 65 ms in some of the participants[21]. Another research showed similar results after 2 Hz stimulation, with latencies depending on the location of the stimulation electrode[22]. Electrodes located superior in the ANT result in the earlier EP latencies.

More literature about stimulation of the subthalamic nucleus (STN) in Parkinsonians exist. In those studies the EPs are divided into short and long-latency responses. Short-latency responses usually occur between 3-8 ms after stimulation[23]. The long-latency response is often described as occurring between 18-25 ms. However, long-latency responses of 29, 70, and 160 ms also occur. This last measurement is done for both Parkinsonians and epileptic patients, showing earlier long-latency evoked potentials, at 25 and 50 ms, compared to 29 and 70 ms for both patients respectively[24]. The exact timings of EPs in literature are variable, which might be due to the different stimulation parameters. Literature about STN stimulation suggests that EPs found between 1-2 ms are generated by antidromic conduction of the hyperdirect pathway[23][15]. Antidromic conduction is conduction along the axon, away from the axon terminal and towards the soma, see Figure 4. It is a movement that is opposite to the more common orthodromic conduction. This is supported by research in which anesthetics are administered, resulting in no change in this 1-2 ms EP compared to disappeared later EPs[25].

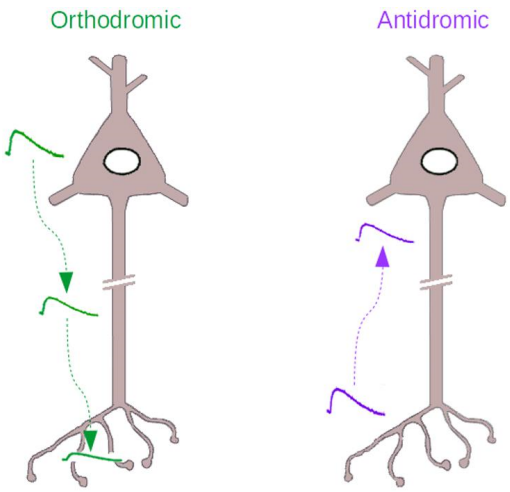

Figure 4: Different types of conduction. Antidromic conduction is conduction along the axon away from the axon terminal and towards the soma. This is likely happening in short-latency (1-2 ms) evoked potentials. Orthodromic conduction is conduction in the opposite direction, towards the axon terminal.

3.4 Source reconstruction

When the functional EEG data is processed and evoked potentials are present in the signal, it is possible to reconstruct the sources responsible for these neural responses[26]. This process can be dissected into two interconnected mathematical challenges: the EEG forward problem and the EEG inverse problem. The forward problem entails simulating the electric potential at the surface of the head generated by microscopic brain activity. In contrast, the inverse problem focuses on reconstructing a spatial distribution of these sources that effectively explains the observed EEG signal. The procedure for assessing the sources comprises three key steps: processing the functional and anatomical data, solving the forward problem and solving the inverse problem on the filtered functional data. An overview of the source reconstruction steps is shown in Figure 5.

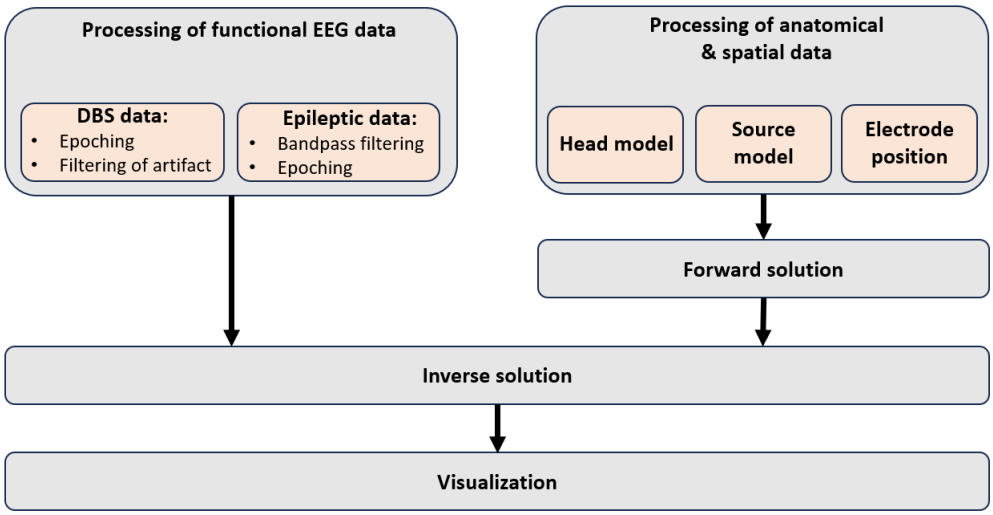

Figure 5: Overview of the steps required for source reconstruction, divided into anatomical MRI and functional EEG data.

3.4.1 Processing of anatomical data

To achieve accurate solutions for both the forward and inverse problems, a comprehensive volume conductor model that accurately replicates the head's geometry is indispensable[26]. The importance of detailed volume conductor models for an accurate inverse analysis has been demonstrated in various studies, especially the positive influence of distinguishing grey matter, white matter, and cerebrospinal fluid (CSF) instead of modeling a homogeneous brain compartment. However, the distinction between skull spongiosa and compacta showed little effect[27]. This segmentation can be translated into a mesh, using a geometrical shape such as a hexahedral or tetrahedral[28]. The type of geometry depends on the best balance between simulation accuracy, computational time, convergence rate, and difficulty in generating a numerical model with a meshing technique. More complex shapes are more accurate, but also more time-consuming. A popular type of geometry shape is a hexahedral. A possible approach to generate a hexahedral mesh is to generate it directly out of the MRIs of the human head[26]. One occurring inaccuracy can be the staircase effect. This effect occurs because the linear elements used in the mesh do not accurately capture the true curvature of the surface. As a result, the visualization or simulation might not reflect the true behavior of the curved geometry, leading to inaccuracies or visual distortions. To avoid staircase effects, geometry-adapted hexahedral meshes can be created in which mesh nodes at tissue boundaries are slightly shifted to obtain a smoother representation of the boundaries. Different conductivity values can be assigned to different tissue types to create a head model. After the creation of the head model, a grid of source positions in the grey matter is created, which is called the source model[29]. The electrodes are aligned to the scalp surface and form the electrode position. Together this forms the forward model. The forward model constrains the solution space for the inverse models that we may wish to apply to our data sets[30]. If we had no constraints at all, there would be an infinite number of solutions that would satisfy the problem that we are trying to solve. By constraining the solution in sensible ways and applying sensible algorithms we can find a unique solution for the inverse model.

Compartments of the head model

The most important compartments of the head model thus consist of white matter, grey matter, CSF, scalp and skull. White matter makes up approximately 60% of the human brain and is found in the deeper tissues[31]. It contains densely packed bundles of myelinated nerve fibers, resulting in the white color. Grey matter comprises approximately 40% of the brain and contains the majority of neuron somas. The grey matter also extends from the brain into the spinal cord. The CSF is located in the brain ventricles and the cranial and spinal subarachnoid spaces[32]. The mean CSF volume is 150 ml, with 25 ml in the ventricles and 125 ml in subarachnoid spaces. The CSF makes up for approximately 12.5% of the full brain volume, which on average contains 1200 ml[33]. A reduction of grey matter has been found from middle age onwards, while the white matter already reduces from young adulthood[34]. Literature also suggests the occurrence of neuronal loss at the seizure focus in temporal lobe epilepsy. Damage to the white matter tracts connecting the focus to extra-focal brain regions results in atrophy observed in anatomically connected but distant brain regions, as noted in previous research[35]. The conductivities of the grey matter, white matter, CSF, skull and scalp are on average 0.33, 0.14, 1.79, 0.01 and 0.43 S/m respectively[26].

3.4.2 Forward solution

In symbolic terms, the EEG forward problem is that of finding, in a reasonable time, the scalp potential at an electrode positioned on the scalp due to a single dipole with a dipole moment and position[36]. The forward problem is stated by the inhomogenous Poisson equation, together with the homogenous Neumann boundary condition[37]:

$$\nabla \cdot (\sigma \nabla u) = \nabla \cdot j^p (= f) \qquad in \;\; \Omega \subseteq \mathbb{R}^3,$$

$$\sigma \nabla u \cdot n = 0 \qquad on \;\; \delta\Omega,$$

where Ω is the volume conductor, and n is the unit outer normal vector on $\delta\Omega$. The EEG forward problem consists of finding the electric potential u along the domain Ω, assuming to know the conductivity profile of the conducting medium (σ) and the primary current (j^p). Solving this equation will lead to the potentials on the scalp for different dipole configurations.

Different numerical methods have been proposed to solve the EEG forward problem including the boundary element method (BEM) and the finite element method (FEM)[26]. BEMs are commonly used in combination with simplified three-layer head models (skin, skull, brain), whereas FEM offers the possibility of modeling more complex geometries, such as skull holes or the strongly folded cortex surface, and tissue conductivity anisotropy without serious influence on computation speed and accuracy[27]. There are some implementations of FEM. One approach is the Venant approach, which can be used to treat the singularity at the right-hand side

of the PDE, introduced by the delta Dirac function representing the dipole[37]. The FieldTrip implementation of the Venant approach is the SimBio method.

3.4.3 Inverse solution

The basic problem of determining the intracranial sources that generate a given EEG measurement over the scalp is the challenge of the inverse problem[38]. A solution to this problem can only be found if a priori assumptions about the sources are incorporated. Neurophysiologic knowledge about the sources of the EEG, biophysical knowledge about how electric activity spreads, anatomic knowledge of the conductive tissues, and knowledge or assumptions about distributions of neuronal activity are all contributors to such a priori constraints. Many different constraints have been introduced over the years and new constraints and assumptions are continuously formulated in the literature based on new available knowledge of signal generation. One method may work well in one particular dataset, but another method may be more suitable another datasets under different conditions. A good knowledge of the properties, advantages, and limitations of each of the methods is essential.

Dipole fitting
Localization of a limited number of equivalent dipoles was the first approach proposed to solve the EEG inverse problem. In this classical approach, the a priori assumption is that only one or a few areas in the brain are active and generate the scalp potential field. Under this constraint, the mathematically best solution can be found by nonlinear optimization. The number of dipoles that can be reliably found is limited by the number of scalp electrodes and by the nonlinear complexity of the search algorithms with multiple sources. Advanced methods, such as decoupling the linear and nonlinear part of the estimation or searching for the best solutions over a certain period with time-varying strength of the dipoles can increase the number of dipoles slightly. Nevertheless, if the number of dipoles is underestimated, the source localization is biased by the missing dipoles, and if too many dipoles are assumed, spurious sources will be introduced. Despite the simplicity and limitation of this a priori assumption, dipole source localization can produce reasonable results under certain conditions, in particular in localizing the epileptic foci[39].

Distributed source imaging
Distributed source imaging methods do not impose a constraint on the number of sources. Instead, a large number (usually more than 5000) of equivalent dipoles are distributed in fixed positions over the whole source space and the strength of each of these dipoles is estimated. Using anatomical information from the individual or a template MRI, the source space is usually constrained to the grey matter. The first and most general linear distributed inverse solution is the minimum norm (MN) solution. The constraint proposed in this solution is that the current distribution over all solution points has minimum energy (minimizing the least-square error) and that the forward solution of this distribution optimally explains the measured data. The constraint of minimal overall energy favors sources closer to the scalp electrodes and overlooks sources in deeper structures. Using different mathematical operations, depth-weighting strategies have been proposed to overcome the problem of favoring superficial sources[40,41].

Beamforming
Beamforming is another spatiotemporal method for source imaging. This method refocuses the signal captured at the scalp to its originating location by finding weights pertaining to each location of the source space, such that the variance of the current dipole at every location is minimal. The magnitude of forward field coefficients decreases with the distance of the dipole to the sensors[42]. This methods deals with a so-called center of head bias which causes the reconstructed power of sources that are far away from the sensors to be a few orders of magnitude larger than the reconstructed power of more superficial sources.

3.5 Research goal

The goal of this research is to find the sources of EPs caused by ANT-DBS, called the 'DBS map', and compare those with the sources of epileptiform discharges, called the 'epilepsy map'. This research goal is based on the hypothesis that a higher map overlap might lead to a higher treatment efficacy. We will include both the long and short-latency responses. To be able to apply source reconstruction on the short-latency response, the DBS artifact needs to be removed. Therefore, a subgoal of this research is to remove the DBS artifact from the EEG data.

3.5.1 Expected results

Based on ANT-DBS literature, we expect to find EPs in the hippocampus after 35-38 ms and/or at 65 ms[21][22]. We also expect to find EPs with latencies between 3-8 ms based on literature about STN stimulation[23]. We used this literature as guidance, due to lack of short-latency ANT-DBS literature. However, variations in the latencies should be expected between the different stimulation locations. Given the connectivity of the anterior nucleus of thalamus (ANT) within the Papez circuit[11], we anticipate identifying the dipole sources of ANT-DBS within this Papez circuit. The distances that are traveled in the circuitry are at most a few centimeters. With a minimum conductance speed of 0.5 m/s, this would result in EPs with a maximum of approximately 100 ms[43].

We expect template subtraction to be the best method for filtering the DBS artifact, based on existing literature showing complete removal of the artifact[15]. The literature dataset is similar to ours, so we expect this method to be applicable and effective for our dataset.

4 Materials and method

This section will describe the materials and methods that were used during this research. First, we will describe the measurement setup and the datasets. Afterwards, we will describe the data analysis including processing of the functional and anatomical data, solving the forward and inverse solution, analysis of the accuracy, and visualization of the results.

4.1 Measurement setup

We used data from the EANSKE study (number R20.053/NL74347.100.20). This study tries to identify biomarkers from local field potentials recorded from the DBS electrodes that are associated with treatment response to DBS in patients with refractory epilepsy. The available data consisted of 20 64-channel DBS-EEG datasets measured at the Medisch Spectrum Twente. The collection of the data was still in progress during this project. Complete datasets contained a baseline measurement before DBS implantation, 1 or 2 days postoperative, and 12 and 24 months postoperative. They also contained a baseline MRI image before DBS implantation and 12 months postoperative. Patients were asked to keep diaries of their perceived seizures during the study period, and they were asked to fill in four questionnaires about psychological well-being at baseline and at 12 and 24 months post-operative. An overview of the measurement setup is shown in Figure 6.

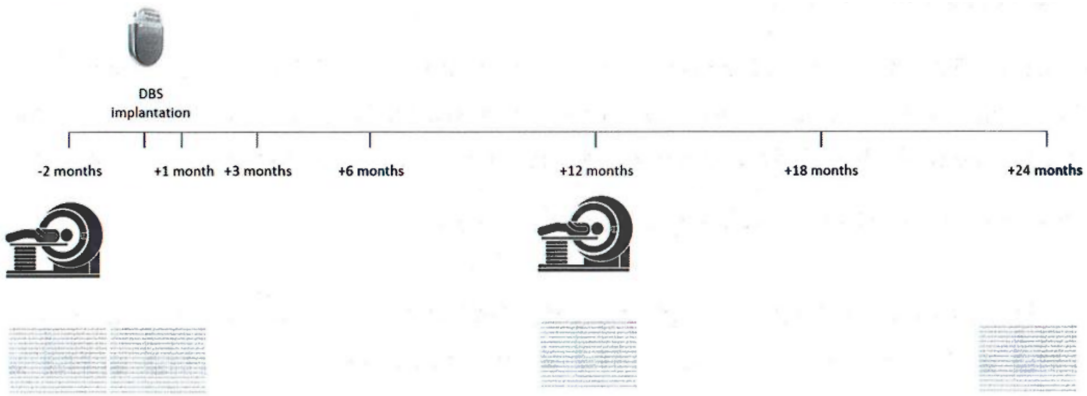

Figure 6: Overview of the measurement setup. MRI scans are made 2 months prior and 12 months after DBS implantation. Four EEG measurements are done: a baseline measurement, one day postoperatively, and at 12 and 24 months.

4.1.1 Materials

For DBS stimulation, implantable Medtronic Model 3389 leads were used, connected to a Medtronic Percept PC Neurostimulator with BrainSense technology. The stimulation pulse is a biphasic, passive charge-balanced pulse, as shown in Figure 7. This means that the stimulation pulse is followed by a charge recovery pulse to result in almost net-zero charge deposition in the tissue. For the EEG measurement, a 64-channel cap with a 10/20 configuration was used.

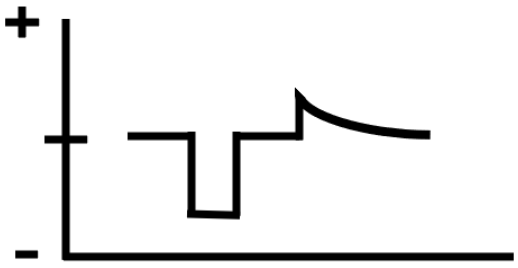

Figure 7: Biphasic passive charge-balanced DBS pulse as used for the data acquisition.

4.2 Data analysis

We analyzed the data in MATLAB (R2023a), with the FieldTrip (20221126) software toolbox for MEG, EEG and iEEG analysis. We used Neurocenter EEG 4.1.4 to visualize raw EEG data. We applied source reconstruction on one patient who had high and low-frequency DBS-EEG data, as well as measured epileptiform discharges in the EEG dataset before DBS implantation. To find the most suitable filtering method, we used six high-frequency, and one low-frequency DBS-ANT stimulation EEG datasets. In this section we will apply the steps as discussed in section 1.4.

4.2.1 Processing of DBS data

We used six high-frequency, and one low-frequency DBS-ANT stimulation EEG datasets to find the most suitable filtering method. The stimulation frequencies vary between 80 and 130 Hz for the high-frequency stimulation. low-frequency stimulation happened at 2 Hz nonsynchronous between the hemispheres. Firstly we loaded the data and assigned the right labels to the right electrodes. Then we removed the electrodes with a zero signal or visually abnormal signal. We found all DBS peaks with the Matlab function `findpeaks`. We epoched high-frequency stimulation datasets between -2 to +10 ms around this DBS peak. The low-frequency stimulation dataset is epoched between -7.5 ms and 242,5 ms around every odd and even DBS peak. This is the maximum time between the DBS peaks. We applied multiple methods to remove the DBS artifact: template subtraction, Hampel filtering and independent component analysis with mutual information.

Template subtraction

We tried to reproduce the results of the article of Peeters et al. using linear interpolation for the first part of the artifact, and template subtraction for the last part of the artifact, as mentioned in section 1.2.4[15]. Firstly, we created a template by averaging the two mastoid electrodes from the start of the passive charge recovery phase of the artifact (for high-frequency stimulation n=13, for low-frequency stimulation n=123) until the end of the epoch. We calculated the relative errors between the individual EEG channels and the template. We averaged these relative errors (RE) over time point 2-5 since this resulted in the best fit. This value is subtracted from 1 to find the scaling factor (SF). We multiplied the scaling factor with the template and subtracted this scaled template from the EEG data. Secondly, we applied linear interpolation from the onset of the artifact until the start of the passive charge recovery phase of the artifact. Linear interpolation is not a very neat method, making it impossible to use the data in this interval. The method only searches for evoked potentials with a latency longer than 3 ms.

Hampel identifier
We used Hampel filtering with an external toolbox[14], with a sliding window consisting of 10 samples. This is often used for Hampel filtering of the DBS artifact. The threshold value is set at t = 3. This threshold value is below the standard value since this showed better results.

Independent component analysis
We applied independent component analysis on the epoched data, to remove the DBS artifact. To make a selection of the components to remove, we used mutual information. Mutual information measures non-linear relations between two random variables[44]. It indicates how much information can be obtained from a random variable by observing another random variable. It is closely linked to the concept of entropy. It is also known as reducing the uncertainty of a random variable if another is known. If the mutual information is zero, that means that the two random variables are independent. The mutual information can be described as follows:

$$I(X;Y) = H(X) + H(Y) - H(X,Y),$$

where I is the mutual information and H is the entropy. $H(X,Y)$ is the joint entropy, which measures the uncertainty when considering two random variables.

Firstly, we applied ICA to our data with the FieldTrip function `ft_componentanalysis`. We used the runica method, which is equivalent to the commonly used Infomax method. The components are visualized with the FieldTrip function `ft_databrowser`, showing both the EEG signal and the distributions over the head belonging to the individual components.

Secondly, we calculated the mutual information between the mastoid electrode, assumingly a clear artifact component, and the remainder components. For this, we used the `Entropy` and `JointEntropy` functions as created by Dwinnel et al[45]. The unit of mutual information is in bins. To make this output value easier interpretable, we converted this to a percentage of overlapping information, by dividing every value with the maximum calculated value of mutual information and multiplying this by 100. We checked the calculated values with the `MutualInformation` function, as created by Dwinnel et al[45], resulting in the same values. Components that contain mutual information above a threshold of 5% are removed from the dataset.

4.2.2 Processing of epileptiform discharges

In this research, we used epileptiform data from one patient before the implantation of DBS. Firstly, we selected two clear focal epileptiform discharges from the Neurocenter software. Secondly, we loaded the EEG dataset in FieldTrip and selected the right time window. The start of the epileptiform discharge is equal to n=1 and ends at n=650 or n=950, for both selections. Each channel received its own label and those with too much noise or no signal are removed. We applied a bandpass filter between 0.5 and 35 Hz, with an order of 2 to the dataset.

4.2.3 Processing anatomical data

In order to use source reconstruction, a head model must be generated. To create a head model of the patient, we loaded a T1-weighted MRI scan into FieldTrip with the function `ft_read_mri`. The dimensions of this loaded dataset are [256x256x160]. We kept the MRI in its native space, and the axes are given an orientation concerning the head. The dataset is resliced and anonymized. We segmented the dataset into grey matter, white matter, CSF, scalp, and skull with the standard settings of the FieldTrip function `ft_volumesegment`. We made a mesh from this segmented dataset, with the function `ft_prepare_mesh` and we used the hexahedral method. To avoid a staircase effect, we applied a maximal shift of 0.3. This shifts vertices at the boundaries in the direction of those hexahedra that represent the minority around them. Finally, we made a head model with the SimBio method and assigned the scalp, skull, CSF, grey, and white matter the conductivities 0.43, 0.001, 1.79, 0.14 and 0.33 S/m respectively. We loaded and fitted a standard FieldTrip 97 channel 10/20 EEG electrode configuration ('standard_1020.elc') over the head model with the function `ft_electrodealign`. We created a source model with the function `ft_prepare_source` model. The resolution of this source model is set at 2 millimeters and the inward shift is set at 1. We also created a simplified BEM model of the brain for visualization purposes.

4.2.4 Forward solution

We calculated and saved the forward solution in a matrix named the leadfield matrix. This matrix is calculated with the function `ft_prepare_leadfield`.

4.2.5 Inverse solution

To solve the inverse problem and find the sources of the generated signals, we used dipole fitting with the function `ft_dipolefitting`. This function uses the previously determined head model and leadfield. We searched for one source per time point, applied a grid search for an initial guess of the dipole parameters, and applied a linear search to optimize those parameters. To have an idea about the accuracy of the source reconstruction pipeline, we first applied source reconstruction on the DBS-EEG artifact. Not much is known about the working mechanism of DBS, but one certainty that we do have is that the source of the artifact should be at the stimulation location, the ANT. The ANT is located at the anterior, superior side of the thalamus, so this is where we would expect to find the dipoles. Subsequently, we applied source reconstruction on DBS-EPs and epileptiform discharges. We chose multiple clear and representative topographies for both the epileptiform data and the DBS-EPs. Those time points are used as input for dipole fitting.

4.2.6 Visualization of the results

The results of the functional data processing are visualized as time series in a Neurocenter layout or as global mean field (GMF) plots. Those GMF plots show the time series of all electrodes in blue and the absolute average of all channels in red. A distribution of the EEG signal over the head is shown in a topoplot. We visualized the anatomical data as a segmentation. The inverse solution is visualized as dipoles in a BEM model of the head, or on an MRI scan for orientation.

5 Results

The whole pipeline is applied to one patient who received high and low-frequency DBS and had visible epileptiform discharges in the EEG dataset before DBS implantation. Additionally, to find the most suitable filtering method, we used six high-frequency ANT-DBS stimulation EEG datasets.

5.1 Processing of the functional data

This section will show the results after processing functional DBS and epileptic EEG data. The output of this section will be the input for source reconstruction.

5.1.1 DBS

We started processing the signal by removing bad channels and epoching around the odd and even peaks and visualized this in Figure 8. The blue lines correspond to the signal of the individual EEG electrodes and the red line corresponds to the absolute average of those electrodes. It clearly shows an artifact, much higher than the physiological neuronal signal. The low-frequency stimulation datasets show long-latency evoked responses, without further processing the data. Those evoked responses occur at 35 ms after averaging both the odd and the even peaks. The processed odd peaks also show an evoked potential at 63 and 157 ms while this is 62, 125, and 180 ms for the even peaks. The DBS-EEG signal of the high-frequency stimulation does not show evoked potentials, only artifact signal. The spatial distribution of this artifact signal is shown in a topoplot.

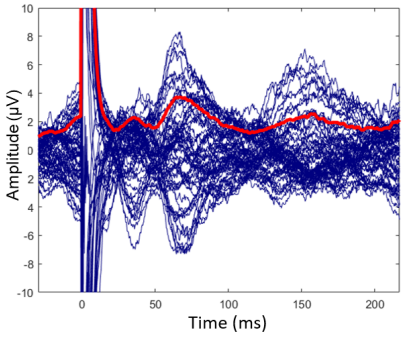

(a) Averaged odd peaks after low-frequency DBS

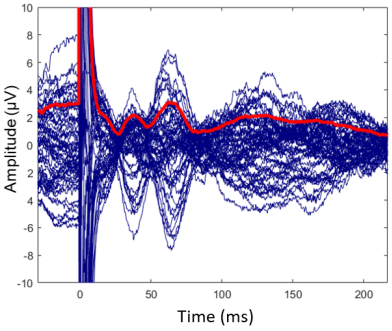

(b) Averaged even peaks after low-frequency DBS

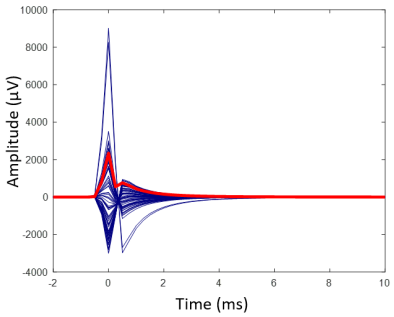

(c) Averaged peaks after high-frequency DBS

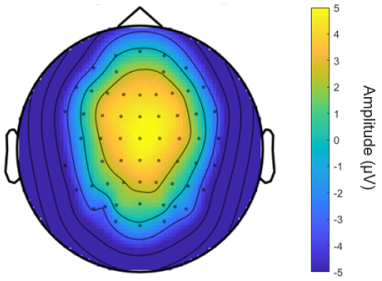

(d) Spatial distribution of the DBS artifact.

Figure 8: DBS-EEG data with a present artifact. Figures 8a and 8b show the time series after stimulation with 2 Hz while averaged over the odd and even peaks respectively. We see a big artifact, but also long-latency evoked potentials. Those evoked potentials occur at 35 ms after averaging both the odd and the even peaks. The processed odd peaks also show an evoked potential at 63 and 157 ms while this is 62, 125 and 180 ms for the even peaks. Figure 8c shows the DBS-EEG data after high-frequency stimulation. The artifact is present, but no evoked potentials are visible. Figure 8d shows the spatial distribution of the EEG signal over the head. The low-frequency stimulation dataset will be used in the source reconstruction pipeline, while this high-frequency dataset only has the purpose of showing the efficacy of the artifact removal methods in the next sections.

Template subtraction

One method to remove the DBS artifact is template subtraction with linear interpolation. The results of this method are shown in Figure 9. More elaborate steps are shown in Appendix A. Applying this method to the low-frequency stimulation datasets results in the appearance of an extra evoked potential at 5.5 ms after stimulation. The method results in evoked potentials at 5.5, 25, 63 and 157 ms for the averaged odd peaks, while this is 5.5, 41, 62, 125 and 180 ms for the averaged even peaks. Filtering the high-frequency stimulation dataset results in a high-frequency noise until 4 ms after stimulation, followed by a smooth signal. The topography at 6 ms after DBS stimulation is clear. However, filtering does not reveal an evoked potential in this dataset.

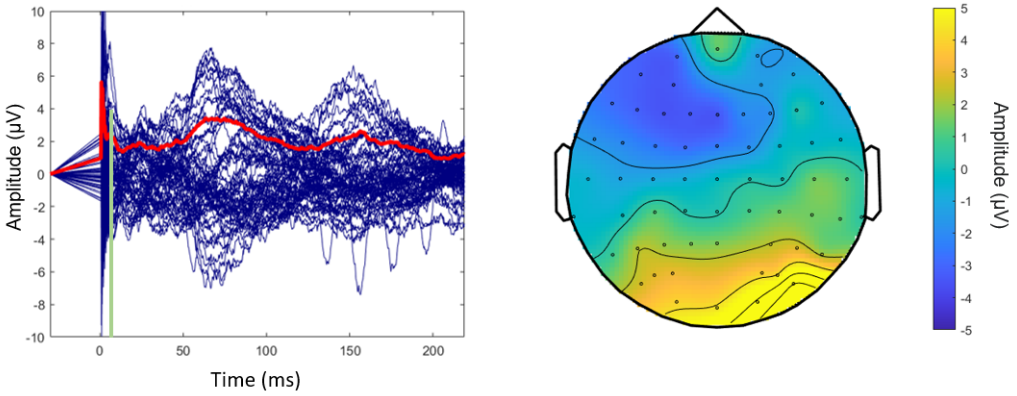

(a) low-frequency DBS averaged around odd peaks

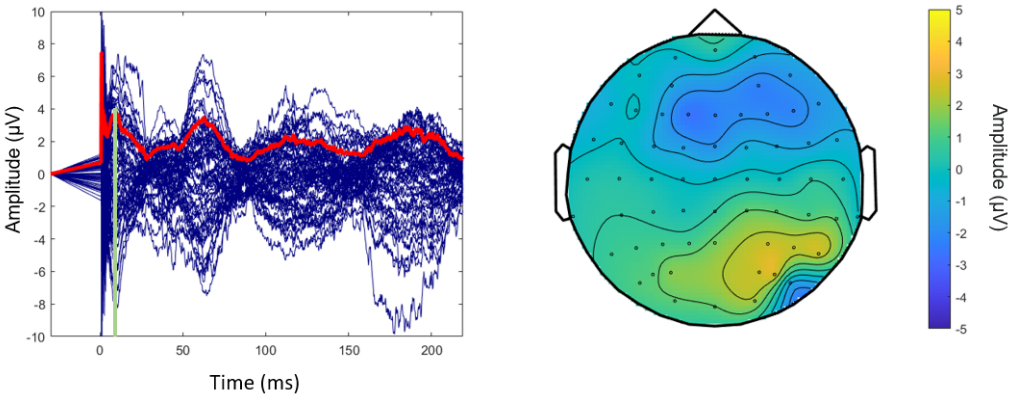

(b) low-frequency DBS averaged around even peaks

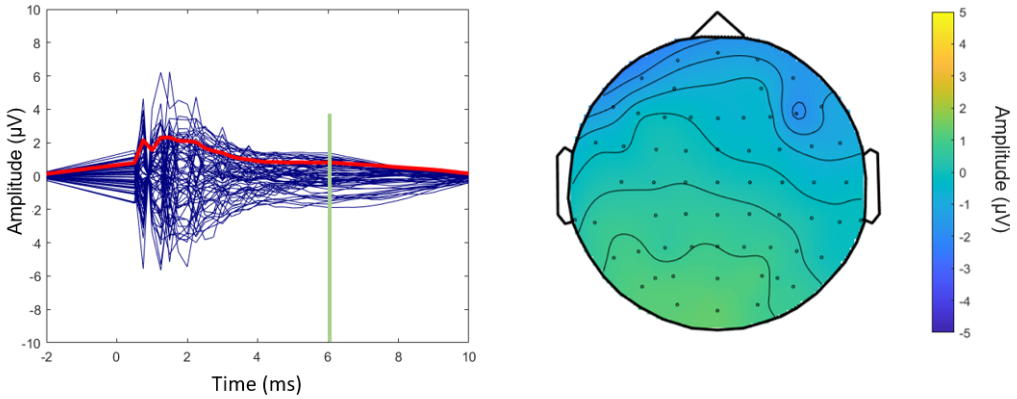

(c) high-frequency DBS

Figure 9: Results of DBS artifact removal methods. Figures 9a and 9b show the result of template subtraction on the low-frequency DBS datasets. An extra evoked potential at 5.5 ms after stimulation appeared in both datasets. The method results in evoked potentials at 5.5, 25, 63 and 157 ms for the averaged odd peaks, while this is 5.5, 41, 62, 125 and 180 ms for the averaged even peaks. Figure 9c shows the filtered high-frequency DBS dataset. High-frequency noise is visible until 4 ms after stimulation, followed by a smooth signal. However, filtering does not reveal an evoked potential in this dataset. The topographies of all datasets at 6 ms after stimulation are showed. They are smooth and do not show signs of an artifact.

Hampel filtering

In this section, we applied a Hampel filter to remove the DBS artifact. The results of this filtering method are shown in Figure 10. The artifact reduced substantially, but the results do not seem to show a physiological brain signal. An extra peak is visible at t=5.5 ms. The topography are not clear and shows mostly noise.

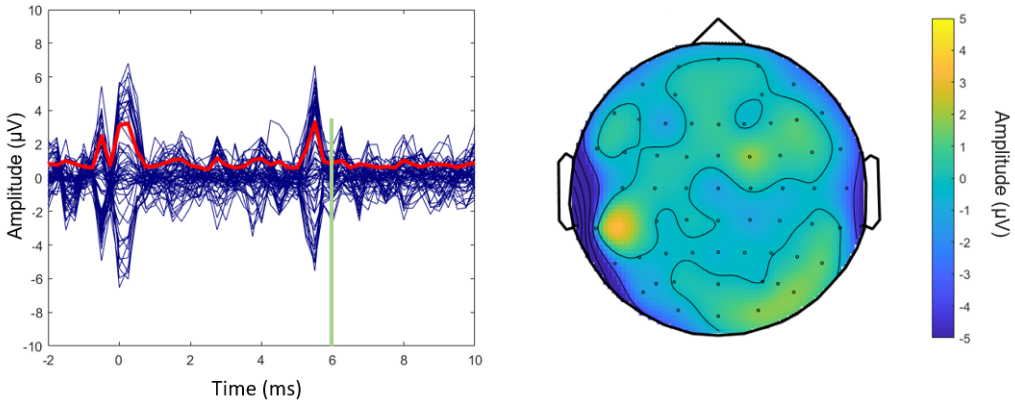

Figure 10: Result of Hampel filtering on a high-frequency DBS-EEG dataset. The artifact reduced substantially, but a noisy, seemingly non-physiological signal is left. An extra peak is visible at t=5.5 ms. The topography at t=6 ms is not smooth and shows mostly noise.

ICA with MI

In this section, we applied independent component analysis on the high-frequency DBS-EEG dataset. We used mutual information to remove artifact components. The artifact reduced, but is still higher in amplitude than the physiological brain signal, see Figure 11. An extra peak is visible at t=6.5 ms. The topography at t=6 ms is clearly caused by the DBS artifact.

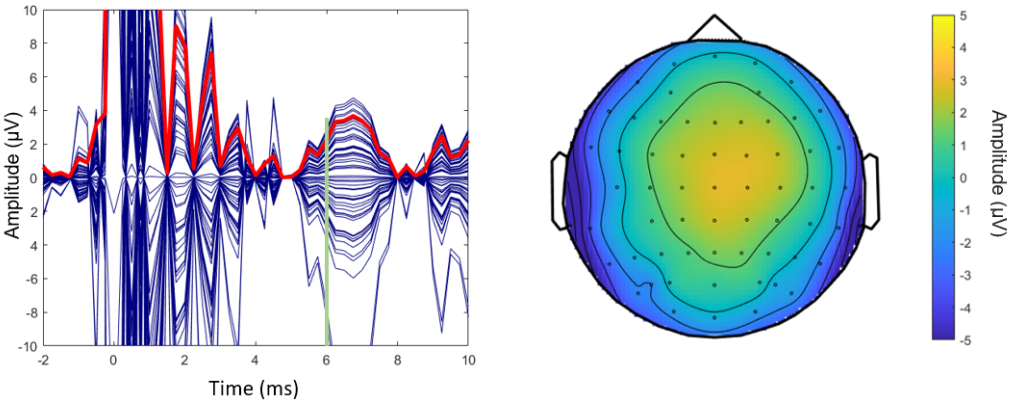

Figure 11: The results of filtering with ICA-MI show a reduction in artifacts, although their amplitude remains higher than that of the physiological brain signal. An additional peak persists at t=6.5 ms, and the topography at t=6 ms is evidently attributed to the DBS artifact.

5.1.2 Epileptiform activity

In addition to the DBS datasets, we also analyzed a dataset with epileptiform discharges. This dataset emanates from the same patient as the low-frequency DBS dataset. The patient shows multiple epileptiform discharges (EDs), annotated by an expert. Those EDs vary in extensiveness. Figure 12 shows results of those EDs. The time series contain three seconds of the recorded bipolar EEG. The red rectangles visualize the moment of the analyzed epileptiform discharge. The times at which we plot the topographies are decided based on visual inspection since they show clear and representative topographies.

The time series and topographies of the first ED are visualized in Figure 20a. The time series show a low-amplitude signal present in only a few EEG channels. The topoplots show activity mostly located focally in the left hemisphere. The time series and topographies of the second ED are visualized in Figure 12b. The time series show a higher-amplitude signal present in more EEG channels. The topoplots show activity with many varying topographies.

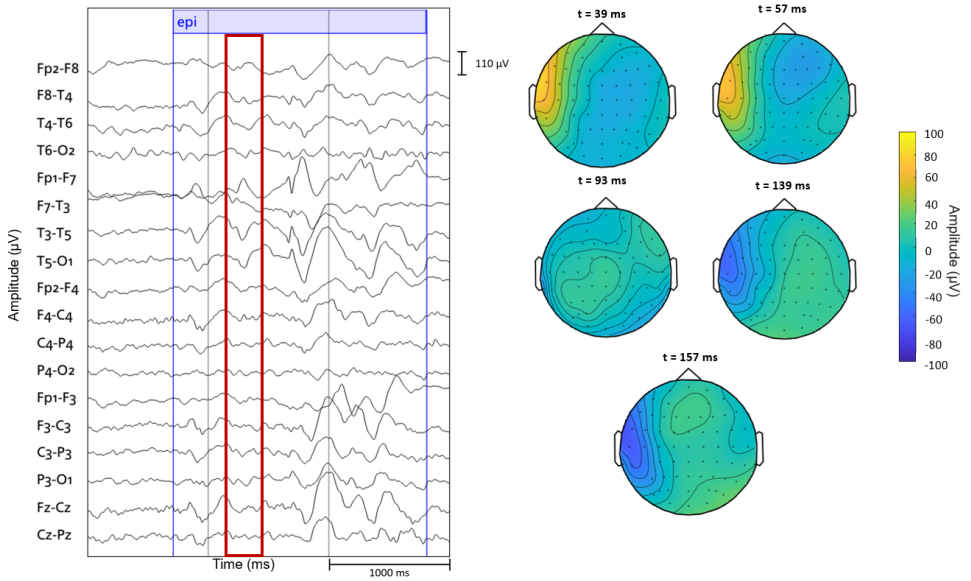

(a) Time series and topographies of the first epileptiform discharge.

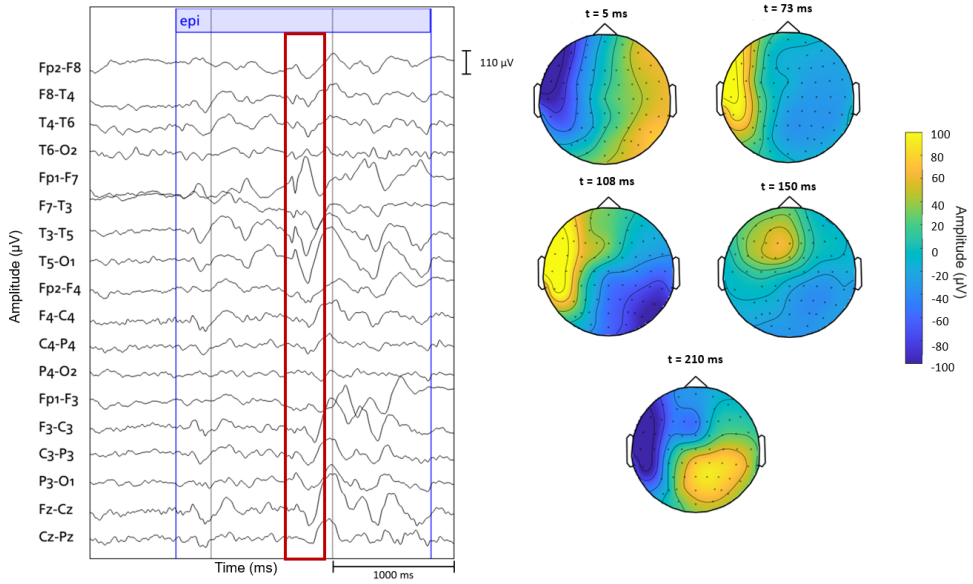

(b) Time series and topographies of the second epileptiform discharge.

Figure 12: Three seconds of a bipolar EEG measurement with visible epileptiform discharges. The red rectangles show the selected moments of the two epileptiform discharges. The moments at which the topographies are shown are selected since they showed clear and representative topographies. Figure 20a shows low-amplitude activity, mostly located focally in the left hemisphere. Figure 12b shows high-amplitude activity, with many varying topographies.

5.2 Processing of anatomical data

Segmentation of the T1-weighted MRI data leads to a result as shown in Figure 13. Landmarks such as the thalamus and the corpus callosum are categorized well. The ventricles and subarachnoid space are visible due to the presence of CSF. The segmented volumes are shown in table 1. As mentioned in chapter 5, the average brain volume is 1300 ml. In our segmentation, this is 1536 ml. This includes CSF, grey and white matter. The CSF should contain approximately 12% of the segmentation. This corresponds to our segmentation, where the CSF contains 7.91% of the volume. The grey and white matter should have a 40:60 ratio respectively. This is the opposite in our segmentation, but might be due to the patient's age, or due to degeneration caused by epilepsy. White matter is visible in deep structures, whereas grey matter is visible in more superficial structures. The source model contains 365904 dipoles inside the grey matter.

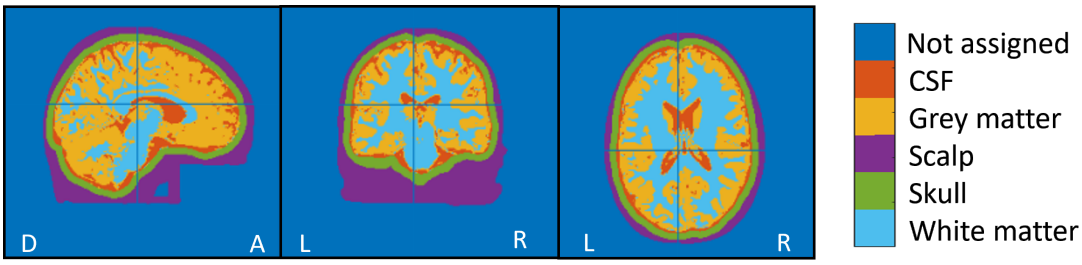

Figure 13: Segmentation of the T1-weighted MRI scan. Landmarks as ventricles, corpus callosum and the thalamus are categorized well.

Segmented volumes	
Segmented structure	**Segmented volume (ml) (% of total)**
White matter	495 (17.56)
Grey matter	847 (30.06)
CSF	223 (7.91)
Scalp	831 (29.48)
Skull	458 (16.26)
Total volume	2818 (100)

Table 1: Segmented volumes of the T1-weighted MRI scan. The brain and CSF volumes correspond to literature. The grey and white matter should have a 40:60 ratio respectively. This is the opposite in our segmentation, but might be due to the patients age, or due to degeneration caused by epilepsy.

5.3 Forward solution

We solved the forward problem which resulted in a leadfield matrix. This matrix relates the generated dipole source in the brain to simulated electric potentials at the surface of the head. Each column of the leadfield matrix corresponds to a sensor, and each row corresponds to a source. The number of sources corresponds to the source model, which is 365904. This leadfield matrix will be used in the next section to solve the inverse solution.

5.4 Inverse solution

After solving the forward problem, we can determine the inverse solution. The first subsection will show the accuracy of the source reconstruction pipeline. Thereafter we will show the first four calculated dipole sources of the DBS-EPs as well as the sources from the epileptiform discharges. In the last subsection, we will compare those results.

5.4.1 Accuracy of the pipeline

In this section, we investigate the accuracy of the pipeline by applying source reconstruction on the DBS-EEG artifact. One ground truth that we have is the stimulation location, namely the ANT. The ANT is located at the anterior, superior side of the thalamus. The calculated dipole sources are visualized in a head model with a segmentation of the thalamus. Those structures are based on a T1-weighted MRI. The anterior (a), posterior (p), superior (s) and inferior (i) sides of the brain are visualized. The red dipole represents the source of the artifact of the averaged odd peaks, while the green dipole represents the source of the artifact of the even peaks. The green dipole is located exactly at the ANT. On the other hand, the red dipole is located a few millimeters more dorsal and inferior compared to the ANT. The circles around the dipoles represent the residual variances of the calculated dipole sources. A bigger circle represents a higher residual variance so less accurate dipole location. The residual variances of both hemispheres are similar.

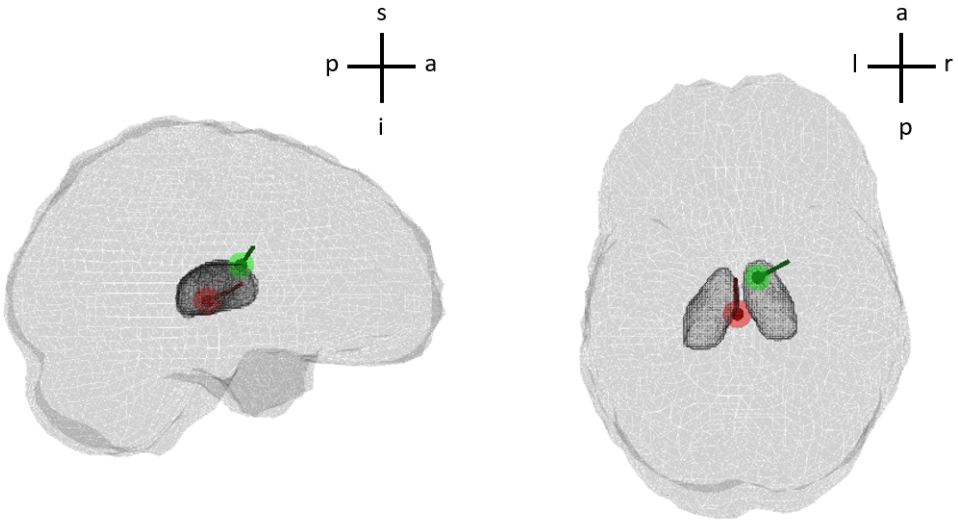

Figure 14: Dipoles as a result of source reconstruction on the DBS-EEG artifact. The calculated dipole sources are visualized in a head model with a segmentation of the thalamus. Those structures are based on a T1-weighted MRI. The anterior (a), posterior (p), superior (s) and inferior (i) sides of the brain are visualized. The red dipole represents the source of the artifact of the averaged odd peaks, while the green dipole represents the source of the artifact of the even peaks. The green dipole is precisely located at the ANT, whereas the red dipole is positioned a few millimeters more dorsal and inferior compared to the ANT. Circles around the dipoles indicate the residual variances of the calculated dipole sources, with a larger circle denoting a higher residual variance and a less accurate dipole location. The residual variances of both hemispheres are comparable."

5.4.2 DBS

This section will discuss the sources generated with source reconstruction of the four DBS-EPs of both the odd and the even peaks. We will discuss all individual EPs based on the global mean fields, topographies and calculated sources. The time at which the topographies are visualized is based on visual inspection. Red resembles source reconstruction on the averaged odd peaks, while green resembles the results of the averaged even peaks. The calculated sources are plotted as dipoles on an MRI for orientation.

Evoked potential 1

The first evoked potential occurs at t=5.5 ms. The topographies show a similar pattern. The dipoles are located superior and anterior to the thalamus. The dipole based on the odd peaks is located lateral in the right hemisphere, while the dipole based on the even peaks is located near the midline.

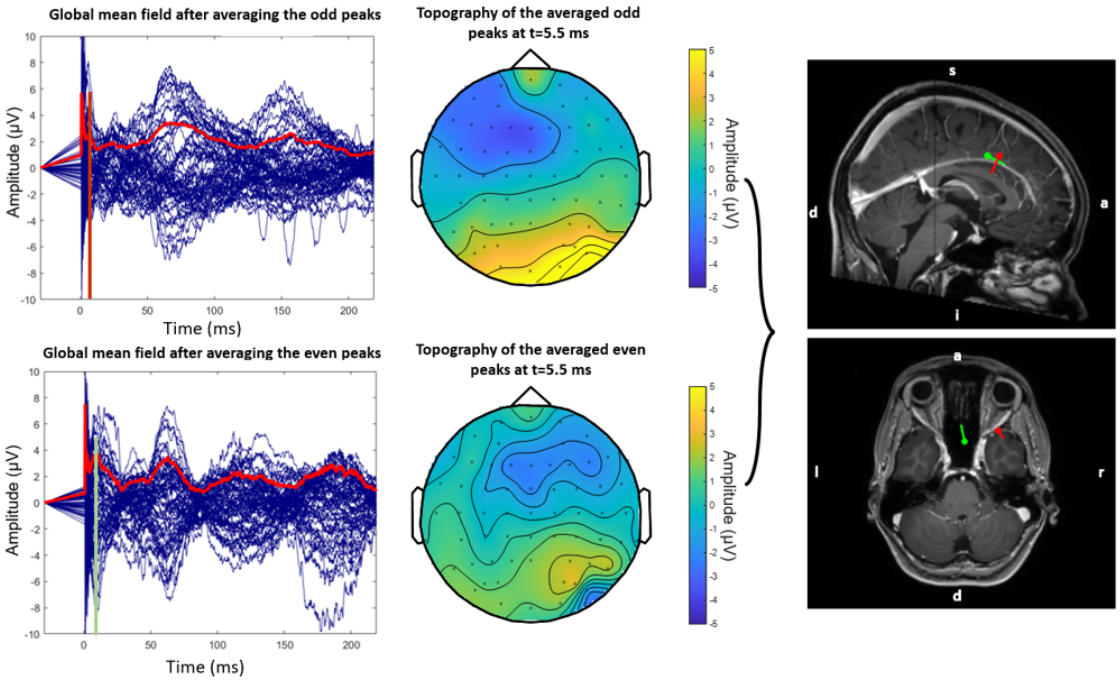

Figure 15: Source reconstruction on the first evoked potential of the odd and even peaks depicted in red and green respectively at a timepoint of 5.5 ms. The topographies demonstrate a similar pattern. The generated dipole sources are visualized on an MRI for spatial reference. It reveals the lateral placement of the odd-peak-based dipole in the right hemisphere and the midline proximity of the even-peak-based dipole.

Evoked potential 2

The second evoked potential occurs at 21 and 41 ms, for the odd and the even peaks respectively. The topographies are different for the odd and even peaks. The dipoles are located anterior to the thalamus and close to the midline.

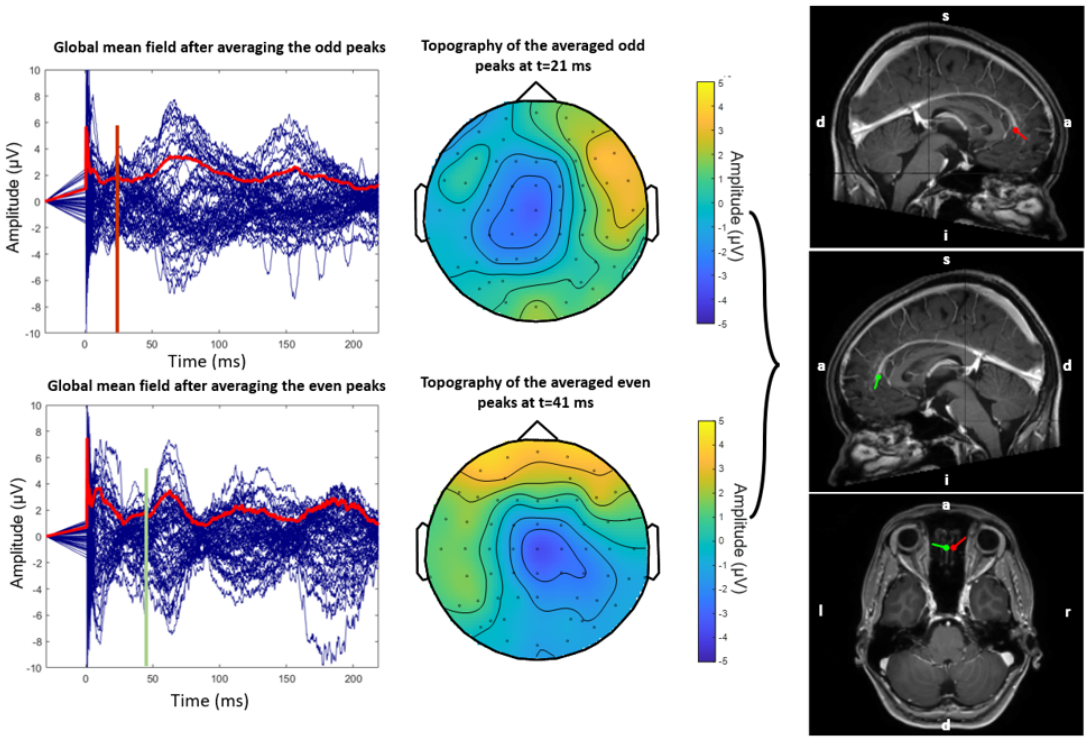

Figure 16: Source reconstruction on the second evoked potential of the odd and even peaks depicted in red and green respectively. The shown time points are 21 ms for the odd dataset and 41 ms for the even dataset. The topographies are different for the odd and even peaks. The generated dipole sources are visualized on an MRI for spatial reference. The dipoles are located anterior to the thalamus and close to the midline.

Evoked potential 3

The third evoked potential occurs at 63 and 62 ms, for the odd and the even peaks respectively. The topoplots show a mirrored effect between the odd and even sources. The dipoles are located near the thalamus in opposite hemispheres. The sources based on the odd peaks are located anterior to the thalamus, while the sources based on the even peaks are located inferior to the thalamus.

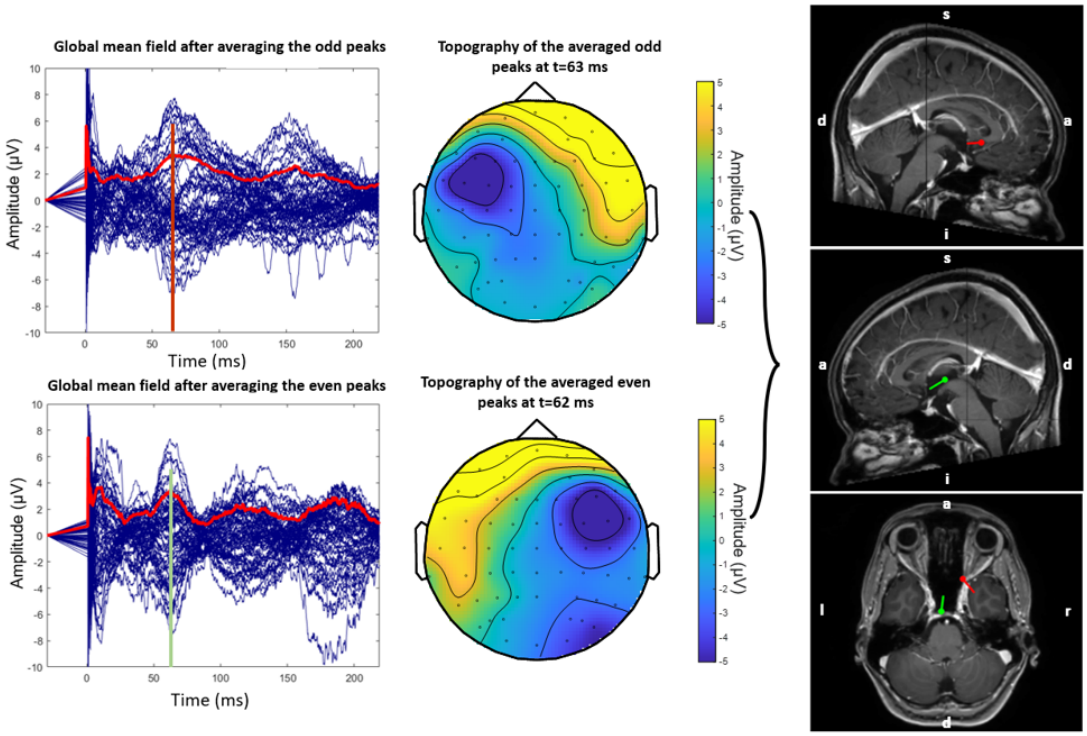

Figure 17: Source reconstruction was performed on the third evoked potential of both odd and even peaks, depicted in red and green, respectively. The displayed time points are 63 ms for the odd dataset and 62 ms for the even dataset. Topoplots illustrate a mirrored effect between the odd and even sources. The resulting dipole sources are visualized on an MRI for spatial reference, positioned near the thalamus in opposite hemispheres. Specifically, sources based on the odd peaks are located anterior to the thalamus, while those based on the even peaks are situated inferior to the thalamus.

Evoked potential 4

The fourth evoked potential occurs at 157 and 125 ms, for the odd and the even peaks respectively. The topographies are different for the odd and even peaks. The dipoles are located inferior and lateral to the thalamus in the right hemisphere.

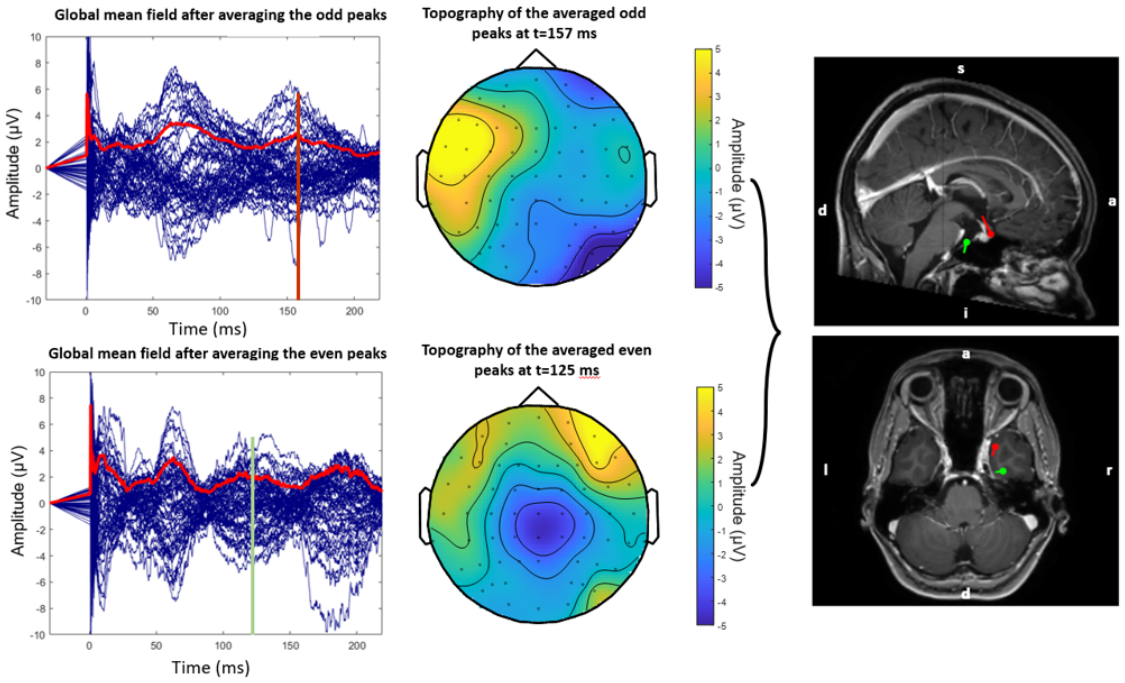

Figure 18: Source reconstruction was conducted on the fourth evoked potential, with odd and even peaks depicted in red and green, respectively. The displayed time points are 157 ms for the odd dataset and 125 ms for the even dataset. Notably, the topographies differ between the odd and even peaks. The resulting dipole sources are visualized on an MRI for spatial reference, situated inferior and lateral to the thalamus in the right hemisphere.

All evoked potentials

Now we combine the previously calculated dipoles. Figure 19 shows the calculated dipoles of the odd and the even peaks respectively on an MRI. This MRI supports the orientation in the head. The different dipole colors represent a different evoked potential.

Both figures depict the temporal progression. The dipoles initiate their movement superior to the thalamus, progressing anteriorly followed by an inferior movement. The dipoles exhibit circular movement around the thalamus. Specifically, the dipoles based on the odd peaks are situated laterally in the right hemisphere. However, the sources of EP 2 and 3 are more medial. On the other hand, the dipoles based on the even peaks are located near the midline, with the last dipole being more lateral.

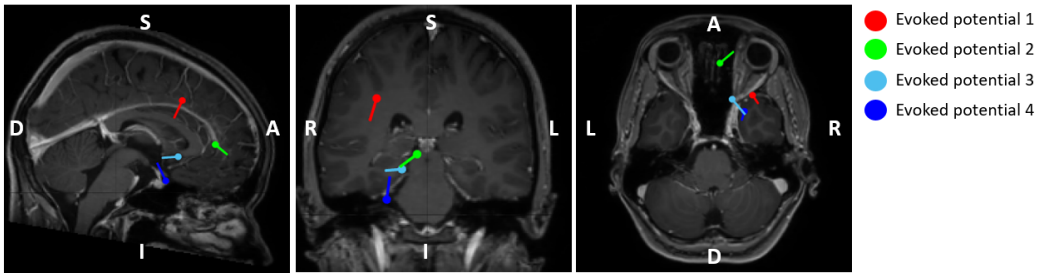

(a) Calculated sources of the odd peaks.

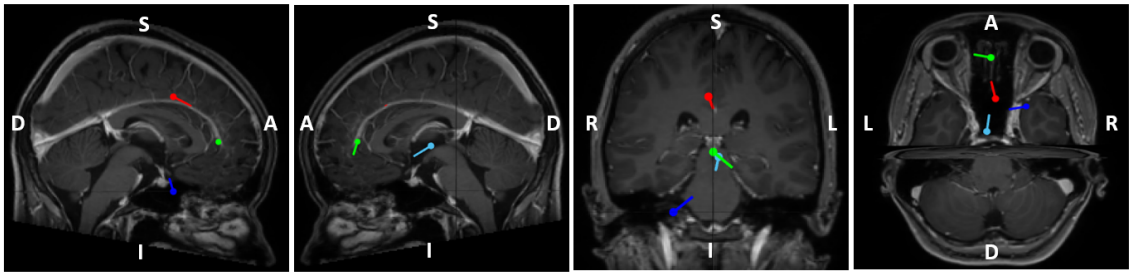

(b) The calculated sources of the even peaks.

Figure 19: The calculated sources of the EPs in both hemispheres. This is a collection of all the previously gathered sources plotted on the patient's T1-weighted MRI. The different colors represent different evoked potentials, showing the progression in time. We see a similar progression in time in both figures, with dipoles moving anteriorly around the thalamus. Figure 19a shows dipoles that are located laterally in the right hemisphere. However, the source of EP 2 and 3 are more medially located. Figure 19b on the other hand shows three dipoles that are located near the midline. Only the last dipole is located in the right hemisphere.

5.4.3 Epileptiform activity

In this section, we analyze the sources of the epileptiform discharges, as shown in Figure 20. The calculated dipole sources are visualized in blue in a head model with a segmentation of the thalamus. Those structures are based on a T1-weighted MRI. The anterior (a), posterior (p), superior (s) and inferior (i) sides of the brain are visualized. Figure 20a shows the results of the first ED, which is low in amplitude and present in only a few channels. The sources of this ED are clearly located focally in the temporal lobe of the left hemisphere. 20b shows source reconstruction on the second ED. This ED is higher in amplitude and the signal is present in more EEG channels. The sources of this ED are clearly located in the temporal and frontal lobes of the left hemisphere. Table 2 shows the distances between the calculated dipoles and the geometric centers of those calculated dipoles per epileptiform discharges. This represents the spread over the left hemisphere. ED 1 shows a minimally smaller spread than ED 2. However, to compensate for the different residual variances, we calculated a weighted average based on the residual variance to determine the spread. The RV is the variance that cannot be explained by our model. Their value can vary between 0 and 1, with 1 being a dipole that does not explain the measured EEG signal at all. A lower residual variance weighs more in this average. We see that the spread of ED 1 is substantially lower than the spread of ED 2.

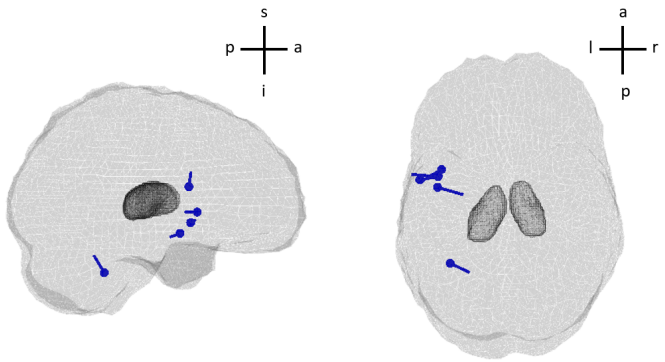

(a) Source reconstruction on the first epileptiform discharge.

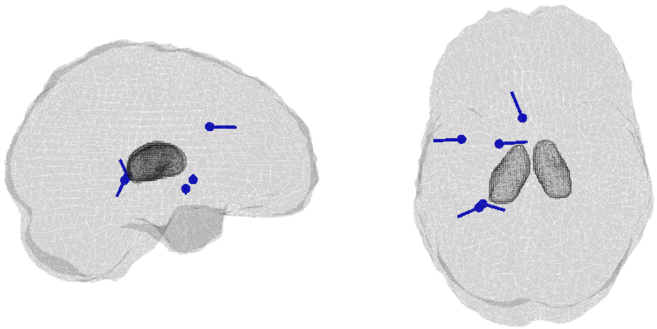

(b) Source reconstruction on the second epileptiform discharge.

Figure 20: Calculated sources of two epileptic discharges in the EEG signal, as shown in section 5.1.2. The calculated sources are visualized as dipoles in a head model with a segmented thalamus. Those structures are based on the T1-weighted MRI of the patient. The anterior (a), posterior (p), superior (s) and inferior (i) sides of the brain are visualized. Different dipoles show the progression through time. Figure 20a shows dipole sources that are localized lateral in the temporal lobe in left hemisphere nearby each other. Figure 20b shows no clear localized source, but a more spread activity in the temporal and frontal lobe of the left hemisphere.

Table 2: Distances between the calculated dipoles and the geometric centers of both epileptiform discharges, showing the spread over the left hemisphere. ED 1 shows a minimally smaller spread than ED 2. However, to compensate for the different residual variances, we calculated a weighted average based on the residual variance to determine the spread. A lower residual variance weights more in this average. We see that the spread of ED 1 is substantially lower than the spread of ED 2.

Spread of epileptiform discharges				
	ED 1		**ED 2**	
Timepoint	Distance to centroid (mm)	1 - Residual variance	Distance to centroid (mm)	1 - Residual variance
1	10.52	0.93	14.81	0.98
2	16.41	0.88	19.86	0.96
3	46.63	0.63	25.11	0.97
4	6.22	0.95	38.30	0.97
5	25.24	0.85	22.47	0.92
Average	21.00		24.11	
Weighted average	19.10		24.13	

5.4.4 Comparison

In this section we will compare the sources of the DBS evoked potentials and the sources of the EDs. First, we will take a look at the residual variances (RV) that we find if we apply source reconstruction. Then we will compare the spatial differences between the EP and ED sources

The residual variances are shown in Table 3. The residual variances of the epileptiform discharges are in general lower than the residual variances of the DBS evoked potentials. Especially the second ED has low RVs. The RVs of evoked potential 1 and 4 are in general higher than the other EPs.

Table 3: Residual variances of the source reconstruction. The RVs of the epileptiform discharges are in general lower than the RVs of the DBS evoked potentials. Especially the second ED has a low RV. The RVs of evoked potential 1 and 4 are in general higher than the RV of the other EPs.

Residual variance of the calculated sources					
DBS peaks			**Epileptiform discharges**		
time point	Odd [0-1]	Even [0-1]	time point	ED 1 [0-1]	ED 2 [0-1]
EP 1	0.355	0.186	1	0.068	0.025
EP 2	0.110	0.106	2	0.120	0.045
EP 3	0.064	0.068	3	0.369	0.035
EP 4	0.431	0.193	4	0.051	0.030
			5	0.150	0.077

Now we will compare the spatial differences between the sources of the DBS-EPs and the EDs. The calculated sources are visualized as dipoles in a head model with a segmented thalamus. Those structures are based on the T1-weighted MRI of the patient. The anterior (a), posterior (p), superior (s) and inferior (i) sides of the brain are visualized. The DBS-EP sources are visualized in orange, while the ED sources are visualized in blue. The size of the dipoles is inversely proportional to the residual variance, resulting a bigger dot for a more reliable source. The centroids are visualized in black. Figure 21a shows a comparison between the DBS-EPs and the first, more focal ED. The distance between the centroids is 51.84 mm and no overlap is visible. Figure 21b shows a comparison between the DBS-EPs and the second, more general ED. For visualization purposes, the dot sizes are multiplied by 0.5. The distance between the centroids is 35.80 mm and the sources show partial overlap. Table 4 shows the average distance between the DBS and epilepsy sources, with a lower average distance between the map sources for ED 2 than ED 1. This supports the partial overlap between the DBS and epilepsy map of ED 2.

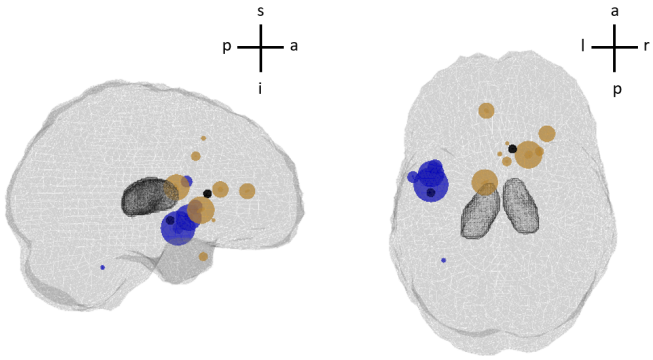

(a) Comparison between the DBS and epilepsy map of the first ED.

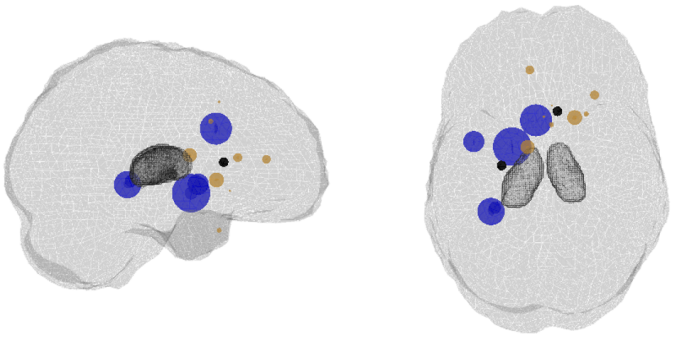

(b) Comparison between the DBS and epilepsy map of the second ED. The dot sizes are multiplied by 0.5, to make the figure more clear.

Figure 21: Comparison between the DBS and epilepsy maps. The estimated sources are visualized as spheres in a head model with a segmented thalamus. Those structures are based on the T1-weighted MRI of the patient. The anterior (a), posterior (p), superior (s) and inferior (i) sides of the brain are visualized. The DBS-EP sources are visualized in orange, while the ED sources are visualized in blue. The size of the dipoles is inversely proportional to the residual variance. A more reliable source is represented as a bigger dot. The centroids are visualized in black. Figure 21a shows no overlap between the maps. The distance between the map centroids is 51.84 mm. Figure 21b shows a partial overlap between the maps. The distance between the centroids is 35.80 mm.

Table 4: Average distance of the ED sources to the sources in the DBS map. The average distance between the map sources is lower for ED 2 than for ED 1, supporting the partial overlap between the DBS and epilepsy map of ED 2.

Distance between the DBS and epilepsy map		
	Average distance between epileptic and DBS sources (mm)	
Time point in the ED	ED 1	ED 2
1	54.79	41.28
2	50.72	53.18
3	87.73	67.60
4	58.60	29.48
5	61.74	64.67
Average	62.72	51.24

6 Discussion

This study explores the overlap between DBS and epilepsy maps in patients with refractory epilepsy, using source reconstruction. After applying template subtraction with linear interpolation to reduce the DBS artifact from the EEG signal, we found four distinct components of ANT-DBS evoked potentials (EPs) at 5.5 (5.5), 25 (41), 63 (62), and 157 (125) ms after averaging the odd (even) DBS peaks. Dipole fitting of these evoked potentials leads to a similar spatial progression in time for the stimulation of the two hemispheres. However, the sources of the odd peaks are laterally localized in the right hemisphere, while the sources of the even peaks are located near the midline, possibly within the circuit of Papez. Source reconstruction conducted on two epileptiform discharges (EDs) from a pre-DBS dataset of the same patient revealed dipoles proximate to each other along the lateral side of the left hemisphere for the first selected ED. Conversely, the results of the second ED demonstrated a greater spread in the left hemisphere. When comparing the DBS and epilepsy maps, only the second ED shows partial overlap with the DBS map. To analyze both long and short-latency responses, we first had to remove the present artifact caused by ANT-DBS. We employed multiple filtering techniques among which template subtraction yielded the best results.

Among the artifact removal methods employed[15,16,19], template subtraction with linear interpolation emerged as the most effective method to notably reduce the DBS artifact. Nevertheless, some physiological brain components might be removed from the signal as well. After applying template subtraction with linear interpolation to our dataset, an extra EP appears at 5.5 ms, corresponding to the results of Peeters et al[15]. However, the earlier visible EPs shift from 35, 63 and 157 ms for the averaged odd peaks to 5.5, 25, 63 and 157 ms. For the averaged even peaks this shifts from 35, 62, 125 and 180 ms to 5.5, 41, 62, 125 and 180 ms. Besides removing the artifact, this filtering technique also has an influence on the latency of the EP at 35 ms, which contradicts our expectation. The last evoked potential of the averaged even peaks is also more prominently visible after filtering. This might indicate that the used template does not only contain artifact components but also physiological brain components.

This is a pioneer research using the combination of ANT-DBS with scalp EEG, artifact removal, and source reconstruction. The literature on EPs following ANT-DBS is scarce, predominantly using depth electrodes. The implementation of source reconstruction on ANT-DBS datasets as well as the investigation of short-latency ANT-DBS EPs is entirely novel. When comparing our results with the literature, we found different EP latencies than the EPs found by Peeter et al[15]. They stimulate the STN, likely activating different brain areas than ANT-DBS. However, they do find early EPs at 3ms. This is supported by other articles showing early EPs at 3-8 ms after stimulation in the subthalamic nucleus in Parkinsonians[23]. From this, we can conclude that both ANT and STN stimulation result in short-latency responses, even though the activated areas are likely different. The found EP latencies do correspond to ANT-DBS literature where EPs were measured with depth electrodes in the hippocampus after 2 Hz stimulation. EPs at 35 or 38 ms, as well as EPs at 65 ms are found in some of the participants[21]. Another research showed similar results after 2 Hz stimulation, with latencies depending on the location of the stimulation electrode[22]. Differences in latencies observed primarily arise from filtering techniques. Additional discrepancies from existing literature may be attributed to the limited size of the dataset. Prior studies typically utilize datasets comprising five patients, whereas this study focuses solely on a single dataset involving low-frequency DBS. Moreover, the stimulation settings vary among patients, potentially resulting in divergent results. The influence of scalp EEG compared to depth electrodes may also contribute to a difference of a few milliseconds. It takes longer for the signal to be measurable at the scalp than in the hippocampus. With this, we would expect to measure the EP with our scalp EEG later than with a depth electrode. The other applied filtering techniques do not remove the artifact completely. A notable observation is that all filtering methods exhibit extra activity around 6 ms. This moment is similar to the extra EP that we found in our low-frequency stimulation dataset. However, the topoplots after applying those filtering methods show noise or artifact topographies.

Source reconstruction applied on the DBS artifact resulted in sources in the ANT for the even peaks, while this was a few millimeters dorsal for the odd peaks. Applying source reconstruction on the artifact is a way to check the accuracy of the pipeline since our stimulation location is in the ANT. This pipeline needs to reach a spatial resolution within the scale of several millimeters so that we can determine the brain structure in which the dipole is located. The deviation from our expectation of source reconstruction on the odd peaks could be caused by the two millimeter spatial resolution that is present in our pipeline, but it could also be possible that the stimulation location is not exactly in the ANT or that a discrepancy occurred between the real electrode placement and the template location. The residual variance of stimulation in both hemispheres is within the same range. Based on the artifact source, we expect an accuracy within the scale of multiple millimeters. However, the artifact amplitude lies within a different range than the evoked potentials and epileptiform discharges, which will lead to different accuracies for those input signals. The accuracy of dipole fitting has been studied, with one elaborate research stimulating the brain with stereo electrodes and measuring the EEG

signal with 21 scalp electrodes[46]. This research found a spatial error between 15 to 25 mm.

While source reconstruction on the EPs caused by stimulation in both hemispheres results in a similar progression around the thalamus, the found dipole sources of the even peaks are more reliable. Both start anterior-superior to the thalamus and move, via the anterior side of the thalamus, towards the inferior side of the thalamus. Due to the connectivity of the ANT within the circuit of Papez[11], we expect to find the ANT-DBS dipole sources in this circuit of Papez. The circuit of Papez moves from the cingulate gyrus to the hippocampus, and back to the ANT. This phenomenon partially corresponds to the movement observed in our visual representations. However, the dipoles derived from the averaged odd peaks are predominantly located laterally within the right hemisphere, whereas those derived from the averaged even peaks are positioned much closer to the midline, resembling the anticipated location of the cingulate gyrus. The last EP based on the even peaks is located more lateral, as we would expect from sources in the hippocampus. To conclude, the dipoles resulting from the averaged even peaks are similar to our expectation based on the literature, but the dipoles based on the averaged odd peaks are located more lateral than expected. We found a higher inaccuracy when applying source reconstruction on the artifact of the odd peaks, which might be the cause of this lateral localization. We also saw higher residual variances (RVs) for source reconstruction on the odd peaks compared to the even peaks, making the results of the even peaks more reliable. The RVs of sources 1 and 4 based on the odd peaks show the highest values as well as the most lateral positions.

Source reconstruction on two epileptiform discharges showed epilepsy maps that are not consistent in time. The first ED showed sources in the temporal lobe of the left hemisphere, with all dipoles relatively close to each other. One source is located further, more dorsal from this focal point. However, this source has a high residual variance compared to the other sources, making this point less reliable than the other dipoles. The second ED showed a more spread signal in the temporal and frontal lobe of the left hemisphere. Those results are similar to the expectations based on the time series since the first ED showed a signal in only a few EEG channels, while the second ED showed a signal in more channels. The patient is diagnosed with bilateral focal epilepsy by the epileptic expertise center SEIN. This is mostly supported by the results from the first ED, even though the dipole sources show a diffuse focal source. The results from the second ED do not support the diagnosis of focal epilepsy. This raises questions about the reliability of source reconstruction on focal epileptic discharges. However, many studies demonstrated the accurate localization of interictal spikes using distributed electric source imaging methods (ESI)[47] such as dipole fitting[39].

The DBS and epilepsy maps showed partial overlap. The second ED shows some overlap with the first EP of the even peaks. The centroid distance between the map of the first ED and the DBS map is larger compared to the second ED. The average distance between the DBS and epilepsy sources is also larger for the first ED. This supports the partial overlap between the DBS and epilepsy map of the second ED. However, this is a simplified method to determine the overlap between the maps. To this timepoint, based on the obtained results no conclusions about whether the selected patient is a responder or non-responder can be drawn. Therefore, we can not yet relate the overlap between maps to the treatment efficacy. The overlap results could be used already as a parameter tuning strategy, trying to find DBS parameters resulting in maps with as much overlap as possible. Another challenge encountered during the comparison of the maps is the presence of numerous EDs in the patients' EEG, displaying considerable variability in the time series. In this study, we selected two EDs that appeared focal. However, when the epilepsy maps exhibit substantial variation, it becomes necessary to establish another method to draw reliable conclusions.

6.1 Limitations and recommendations

This study has a series of limitations. Firstly, when applying template subtraction with linear interpolation, the latency of the second EP shifts. This method is based on removing only the artifact components and leaving in all the physiological components. We used the average of the two mastoid electrodes as a template. However, there is no guarantee that the mastoid electrodes are free of physiological brain signal, which could potentially contribute to changes in the residual signal. A solution could be using a template measured with a higher distance from the brain for a higher guarantee of the absence of physiological brain signals.

Source reconstruction revealed discrepancies between the amount in which the dipoles are located to the lateral side of the hemisphere. This contradicts the expected symmetry in Papez's circuit. One potential cause could be inaccuracies in electrode placement during the reconstruction pipeline. For this pipeline, we use patient-based anatomical data to create a head model, but we use a template for the electrode positions. Small shifts in electrode positions can have a considerable influence on the sources that we found. A solution for this problem would be to map the electrode positions so that this becomes also patient-specific data. This will be applied to patients who in the future will be included in this research. For those measurements, we will make use of FieldTrips 3D scanner software[48].

Another limitation of this study is the stimulation frequency that deviates from the clinical setting. We changed the stimulation frequency temporarily to 2 Hz, to measure long-latency responses. However, in a clinical setting, this would be at least 80 Hz[8]. We already saw differences between the short-latency responses at 5.5-6 ms, which were present in low-frequency stimulation, but not clearly in high-frequency stimulation. It is important to check whether the same connections are activated similarly for those different stimulation settings. It is possible with the currently available datasets to compare the 6 ms EPs of the high and low-frequency DBS datasets. This remained pending due to time constraints but could gather a first insight into the influence of the stimulation frequency. To analyze this more thoroughly, an amendment to the research protocol has been submitted and approved. In the future, we will change more stimulation parameters such as stimulation frequency, amplitude, and stimulation electrode. We hope to gather more insight into the influence of those parameters on the DBS signal.

The source reconstruction method that we applied is dipole fitting. One limitation of this method is the assumption that the signal is caused by only one dipole at each time point[38]. However, multiple areas in the brain can be activated simultaneously. The results of dipole fitting might as well be an average of the actual dipoles responsible for the measured brain activity. This limitation necessitates caution in interpreting reconstructed sources. We applied dipole fitting due to its simplicity and the ability to check progression over time. A solution to this assumption could be to determine the number of the equivalent dipole sources corresponding to the scalp EEG as described by Bai et al[49]. This method can estimate the number of dipole sources from instantaneous scalp EEG distribution for up to three dipoles. Other source reconstruction techniques that assume a distributed source exist, such as minimum norm estimation (MNE) and beamforming. Those methods have the disadvantage of a bias towards deep or superficial structures. Variations exist to solve those biases. Currently widely used variations of the MNE solution are for example eLORETA[40] or sLORETA[41]. The depth bias of beamforming can be solved by applying a location-specific normalization[42]. The spread of the dipole sources of the focal epileptic discharges raises the question of whether a method assuming a distributed source would better represent the physiology. Applying multiple source reconstruction techniques could be a way to check the accuracy of the pipeline. If multiple methods show similar results, it is more likely that the results are accurate.

In applying source reconstruction to the DBS dataset, we observed that the source of averaged odd peaks is a few millimeters dorsal compared to the ANT. This might be due to inaccuracies or the two-millimeter spatial resolution that is included in this pipeline. However, another possibility would be that the stimulation location is not exactly in the ANT. We could check this by plotting the source reconstruction results over the CT scan, which shows the implanted electrodes. With this, we could also determine the exact error between the dipole and the source location. We would also expect the signal to be symmetric based on the literature. To see how symmetric the signal is, we could subtract the signal of one hemisphere from the signal of the other hemisphere.

We selected time points in the EPs to apply source reconstruction, based on how clear their topographies were. Instead of picking those moments visually, we could have selected time points with low residual variances, since this implies little noise. An alternative approach could involve using a single source to interpret the signal until its predictive accuracy diminishes. At that moment we recalculate the best dipole source. This alternative method offers a potentially more physiological representation of signal progression.

Another future recommendation could be found in the processing of the epileptiform discharges. We found two different epilepsy maps for the different EDs, making it challenging to interpret whether the maps are overlapping. Multiple possibilities are available when selecting the EDs. One possibility is to select the epilepsy map that is most often present in the patient. Another option would be to create one big epilepsy map, without a distinction of EDs. Literature sometimes strives for a higher signal-to-noise ratio by averaging multiple similar-shaped EDs[50]. This could lead to a more consistent epilepsy map but comes with the risk of data loss. In order to state the most suitable selection pipeline, more data are needed including the patients' treatment efficacy.

The ANT-DBS and ED sources are visualized and compared as dots, which presents challenges in interpretation. The centroid distances and average distances between map sources are used as a measure of overlap. However, this is a very simplified method. A more effective approach would involve employing head parcellations, readily available in numerous atlases[51]. By utilizing these atlases, we can identify the activated brain structures, simplifying the assessment of overlap and facilitating a clearer understanding of the data.

Lastly, more patients should be included in this research. For now, we only applied filtering on six datasets, and source reconstruction on one pre-DBS and one post-DBS dataset. More data is being gathered to make this possible in the future. These patients will be measured according to the new amendment in the protocol as described in the previous paragraph.

7 Conclusion

This research sheds light on estimated dipole sources of ANT-DBS evoked potential measured at the scalp and their progression over time. It also looks into dipole sources of epileptiform discharges of the same patient. To reach this goal, the optimal filter to reduce DBS artifacts was found.

The best filtering technique was template subtraction which led us to EPs at 5.5, 25, 63, and 157 ms for averaged odd peaks and 5.5, 41, 62, 125 and 180 ms for averaged even peaks. Source reconstruction on these EPs after stimulation of one hemisphere leads to dipoles which possibly follow the circuit of Papez, as would be expected based on the literature. However, stimulation in the other hemisphere results in dipole sources located more lateral, which can be explained by higher residual variances and inaccuracy at baseline testing. Source reconstruction on EDs leads to focal or more spread dipoles in the left hemisphere. Partial overlap is found between the DBS and epilepsy maps. Additional research is crucial to establish robust conclusions regarding DBS and epilepsy map overlaps. However, the insights gained from this research could play a pivotal role in influencing epilepsy treatment strategies, introducing a predictive parameter for assessing the treatment efficacy of ANT-DBS in refractory epileptic patients.

References

[1] K. L. Dell, M. J. Cook, and M. I. Maturana, "Deep brain stimulation for epilepsy: Biomarkers for optimization," *Current Treatment Options in Neurology*, vol. 21, pp. 1–16, 10 2019.

[2] C. E. Stafstrom and L. Carmant, "Seizures and epilepsy: An overview for neuroscientists," *Cold Spring Harbor Perspectives in Medicine*, vol. 5, pp. 1–19, 2015.

[3] "Types of seizures | epilepsy | cdc."

[4] S. Flynn and M. A. Babi, "Anticonvulsants," *Pharmacology and Therapeutics for Dentistry: Seventh Edition*, pp. 176–192, 9 2016.

[5] H. F. González, A. Yengo-Kahn, and D. J. Englot, "Vagus nerve stimulation for the treatment of epilepsy," *Neurosurgery Clinics of North America*, vol. 30, pp. 219–230, 4 2019.

[6] V. Litvak, E. Florin, G. Tamás, S. Groppa, and M. Muthuraman, "Eeg and meg primers for tracking dbs network effects," *NeuroImage*, vol. 224, p. 117447, 1 2021.

[7] T. J. Foutz and M. Wong, "Brain stimulation treatments in epilepsy: Basic mechanisms and clinical advances," *Biomedical Journal*, vol. 45, pp. 27–37, 2 2022.

[8] V. Salanova, T. Witt, R. Worth, T. R. Henry, R. E. Gross, J. M. Nazzaro, D. Labar, M. R. Sperling, A. Sharan, E. Sandok, A. Handforth, J. M. Stern, S. Chung, J. M. Henderson, J. French, G. Baltuch, W. E. Rosenfeld, P. Garcia, N. M. Barbaro, N. B. Fountain, W. J. Elias, R. R. Goodman, J. R. Pollard, A. I. Tröster, C. P. Irwin, K. Lambrecht, N. Graves, and R. Fisher, "Long-term efficacy and safety of thalamic stimulation for drug-resistant partial epilepsy," *Neurology*, vol. 84, p. 1017, 3 2015.

[9] Y. C. Wu, Y. S. Liao, W. H. Yeh, S. F. Liang, and F. Z. Shaw, "Directions of deep brain stimulation for epilepsy and parkinson's disease," *Frontiers in Neuroscience*, vol. 15, p. 680938, 6 2021.

[10] A. Vetkas, J. Germann, G. Elias, A. Loh, A. Boutet, K. Yamamoto, C. Sarica, N. Samuel, V. Milano, A. Fomenko, B. Santyr, J. Tasserie, D. Gwun, H. H. Jung, T. Valiante, G. M. Ibrahim, R. Wennberg, S. K. Kalia, and A. M. Lozano, "Identifying the neural network for neuromodulation in epilepsy through connectomics and graphs," *Brain Communications*, vol. 4, 2022.

[11] A. J. Nelson, "The anterior thalamic nuclei and cognition: A role beyond space?," *Neuroscience and Biobehavioral Reviews*, vol. 126, p. 1, 7 2021.

[12] A. Kamali, S. Milosavljevic, A. Gandhi, K. R. Lano, P. Shobeiri, F. G. Sherbaf, H. I. Sair, R. F. Riascos, and K. M. Hasan, "The cortico-limbo-thalamo-cortical circuits: An update to the original papez circuit of the human limbic system," *Brain Topography 2023 36:3*, vol. 36, pp. 371–389, 4 2023.

[13] J. P. Aggleton, A. J. Nelson, and S. M. O'Mara, "Time to retire the serial papez circuit: Implications for space, memory, and attention," *Neuroscience Biobehavioral Reviews*, vol. 140, p. 104813, 9 2022.

[14] G. Lio, S. Thobois, B. Ballanger, B. Lau, and P. Boulinguez, "Removing deep brain stimulation artifacts from the electroencephalogram: Issues, recommendations and an open-source toolbox," *Clinical Neurophysiology*, vol. 129, pp. 2170–2185, 10 2018.

[15] J. Peeters, A. Boogers, T. V. Bogaert, H. Davidoff, R. Gransier, J. Wouters, B. Nuttin, and M. M. Laughlin, "Electrophysiologic evidence that directional deep brain stimulation activates distinct neural circuits in patients with parkinson disease," *Neuromodulation: Technology at the Neural Interface*, vol. 26, pp. 403–413, 2 2023.

[16] D. P. Allen, E. L. Stegemöller, C. Zadikoff, J. M. Rosenow, and C. D. MacKinnon, "Suppression of deep brain stimulation artifacts from the electroencephalogram by frequency-domain hampel filtering," *Clinical Neurophysiology*, vol. 121, pp. 1227–1232, 8 2010.

[17] D. P. Allen, "A frequency domain hampel filter for blind rejection of sinusoidal interference from electromyograms," *Journal of Neuroscience Methods*, vol. 177, pp. 303–310, 3 2009.

[18] A. L. Kandemir, V. Litvak, and E. Florin, "The comparative performance of dbs artefact rejection methods for meg recordings," *NeuroImage*, vol. 219, p. 117057, 10 2020.

[19] A. Tharwat, "Independent component analysis: An introduction," *Applied Computing and Informatics*, vol. 17, pp. 222–249, 2018.

[20] Y. Challenor, E. Gonzalez, and A. Cassvan, "Evoked potentials," *The Physiological Basis of Rehabilitation Medicine*, pp. 283–285, 1994.

[21] Y. C. Wang, V. Kremen, B. H. Brinkmann, E. H. Middlebrooks, B. N. Lundstrom, S. S. Grewal, H. Guragain, M. H. Wu, J. J. V. Gompel, B. T. Klassen, M. Stead, and G. A. Worrell, "Probing circuit of papez with stimulation of anterior nucleus of the thalamus and hippocampal evoked potentials," *Epilepsy Research*, vol. 159, p. 106248, 1 2020.

[22] J. J. V. Gompel, B. T. Klassen, G. A. Worrell, K. H. Lee, C. Shin, C. Z. Zhao, D. A. Brown, S. J. Goerss, B. A. Kall, and M. Stead, "Anterior nuclear deep brain stimulation guided by concordant hippocampal recording," *Neurosurgical Focus*, vol. 38, p. E9, 6 2015.

[23] A. Devergnas and T. Wichmann, "Cortical potentials evoked by deep brain stimulation in the subthalamic area," *Frontiers in Systems Neuroscience*, vol. 5, 5 2011.

[24] K. B. Baker, E. B. Montgomery, A. R. Rezai, R. Burgess, and H. O. Lüders, "Subthalamic nucleus deep brain stimulus evoked potentials: Physiological and therapeutic implications," *Movement Disorders*, vol. 17, pp. 969–983, 9 2002.

[25] S. Li, G. W. Arbuthnott, M. J. Jutras, J. A. Goldberg, and D. Jaeger, "Resonant antidromic cortical circuit activation as a consequence of high-frequency subthalamic deep-brain stimulation," *Journal of Neurophysiology*, vol. 98, pp. 3525–3537, 12 2007.

[26] J. Vorwerk, R. Oostenveld, M. C. Piastra, L. Magyari, and C. H. Wolters, "The fieldtrip-simbio pipeline for eeg forward solutions," *BioMedical Engineering Online*, vol. 17, 3 2018.

[27] J. Vorwerk, J. H. Cho, S. Rampp, H. Hamer, T. R. Knösche, and C. H. Wolters, "A guideline for head volume conductor modeling in eeg and meg," *NeuroImage*, vol. 100, pp. 590–607, 10 2014.

[28] "Hexahedral mesh vs. tetrahedral: Comparing high-quality meshing | system analysis blog | cadence."

[29] "Solving the eeg and meg forward problem using the finite element method - fieldtrip toolbox."

[30] T. F. Oostendorp and A. V. Oosterom, "Source parameter estimation in inhomogeneous volume conductors of arbitrary shape," *IEEE Transactions on Biomedical Engineering*, vol. 36, pp. 382–391, 1989.

[31] A. A. Mercadante and P. Tadi, "Neuroanatomy, gray matter," *StatPearls*, 7 2023.

[32] L. Sakka, G. Coll, and J. Chazal, "Anatomy and physiology of cerebrospinal fluid," *European Annals of Otorhinolaryngology, Head and Neck Diseases*, vol. 128, pp. 309–316, 12 2011.

[33] R. Purkait, "Growth of cranial volume: an anthropometric study," *Journal of plastic, reconstructive aesthetic surgery : JPRAS*, vol. 64, 5 2011.

[34] A. Giorgio, L. Santelli, V. Tomassini, R. Bosnell, S. Smith, N. D. Stefano, and H. Johansen-Berg, "Age-related changes in grey and white matter structure throughout adulthood," *NeuroImage*, vol. 51, pp. 943–951, 7 2010.

[35] C. Scanlon, S. G. Mueller, I. Cheong, M. Hartig, M. W. Weiner, and K. D. Laxer, "Grey and white matter abnormalities in temporal lobe epilepsy with and without mesial temporal sclerosis," *Journal of neurology*, vol. 260, pp. 2320–2329, 9 2013.

[36] H. Hallez, B. Vanrumste, R. Grech, J. Muscat, W. D. Clercq, A. Vergult, Y. D'Asseler, K. P. Camilleri, S. G. Fabri, S. V. Huffel, and I. Lemahieu, "Review on solving the forward problem in eeg source analysis," *Journal of NeuroEngineering and Rehabilitation*, vol. 4, pp. 1–29, 11 2007.

[37] M.-C. 'Piastra, "New finite element methods for solving the meg and the combined meg/eeg forward problem," 2019.

[38] C. M. Michel and B. He, "Eeg source localization," *Handbook of Clinical Neurology*, vol. 160, pp. 85–101, 1 2019.

[39] G. Akdeniz, "Verification of dipole fit source localization in patients with epilepsy using postoperative mri," *Neurology Asia*, vol. 23, pp. 7–15, 2018.

[40] T. Halder, S. Talwar, A. K. Jaiswal, and A. Banerjee, "Quantitative evaluation in estimating sources underlying brain oscillations using current source density methods and beamformer approaches," *eNeuro*, vol. 6, 7 2019.

[41] O. Hauk, D. G. Wakeman, and R. Henson, "Comparison of noise-normalized minimum norm estimates for meg analysis using multiple resolution metrics," *Neuroimage*, vol. 54, p. 1966, 2 2011.

[42] B. U. Westner, S. S. Dalal, A. Gramfort, V. Litvak, J. C. Mosher, R. Oostenveld, and J. M. Schoffelen, "A unified view on beamformers for m/eeg source reconstruction," *NeuroImage*, vol. 246, p. 118789, 2 2022.

[43] D. Purves, G. J. Augustine, D. Fitzpatrick, L. C. Katz, A.-S. LaMantia, J. O. McNamara, and S. M. Williams, "Increased conduction velocity as a result of myelination," 2001.

[44] P. Aznar, "What is mutual information? | quantdare."

[45] W. Dwinnel, "Mutual information - file exchange - matlab central."

[46] K. Unnwongse, S. Rampp, T. Wehner, A. Kowoll, Y. Parpaley, M. V. Lehe, B. Lanfer, M. Rusiniak, C. Wolters, and J. Wellmer, "Validating eeg source imaging using intracranial electrical stimulation," *Brain Communications*, vol. 5, 12 2022.

[47] V. Brodbeck, L. Spinelli, A. M. Lascano, M. Wissmeier, M. I. Vargas, S. Vulliemoz, C. Pollo, K. Schaller, C. M. Michel, and M. Seeck, "Electroencephalographic source imaging: a prospective study of 152 operated epileptic patients," *Brain*, vol. 134, p. 2887, 2011.

[48] S. Homölle and R. Oostenveld, "Using a structured-light 3d scanner to improve eeg source modeling with more accurate electrode positions," *Journal of Neuroscience Methods*, vol. 326, 10 2019.

[49] X. Bai and B. He, "On the estimation of the number of dipole sources in eeg source localization," *Clinical neurophysiology : official journal of the International Federation of Clinical Neurophysiology*, vol. 116, p. 2037, 9 2005.

[50] V. S. Dimakopoulos, M. Antonakakis, G. Moeddel, J. Wellmer, S. Rampp, M. Zervakis, and C. H. Wolters, "Combined eeg/meg source reconstruction of epileptic activity using a two-phase spike clustering approach," *Proceedings - 2019 IEEE 19th International Conference on Bioinformatics and Bioengineering, BIBE 2019*, pp. 877–881, 10 2019.

[51] "Corticalparcellation - free surfer wiki."

A Template subtraction with linear interpolation

This section will give further details about template subtraction with linear interpolation on a high-frequency DBS dataset, as described in section 4.2.1

We initiated the analysis by constructing a template through the averaging of signals from the mastoid electrodes. In the visual representation of Figure 22, the template is delineated in red, while all other EEG channels are depicted in blue.

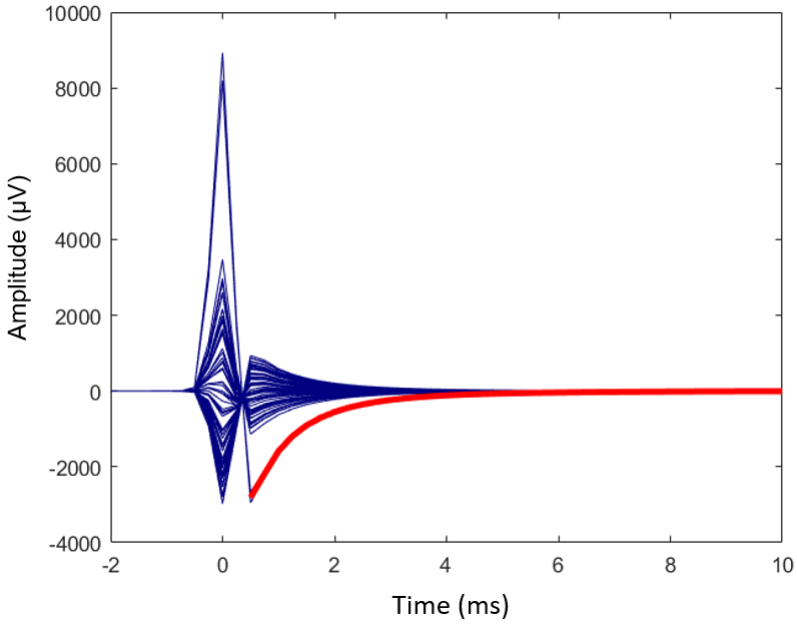

Figure 22: The red line in the figure represents our template, derived from the average of mastoid electrodes. Notably, the template exhibits a higher amplitude in comparison to the other channels, illustrated by the blue lines.

To facilitate template subtraction, scaling was necessary for the integration of this template. The fitting process involved aligning the template with the EEG signal, based on time points 2-5 during the onset of the passive charge recovery phase. In Figure 23, the results of this fitting process for channel FP1 are depicted. Remarkably, the fitting demonstrates a commendable overlap between the template and the EEG channel. However, a noticeable deviation occurs at the initiation point of the template.

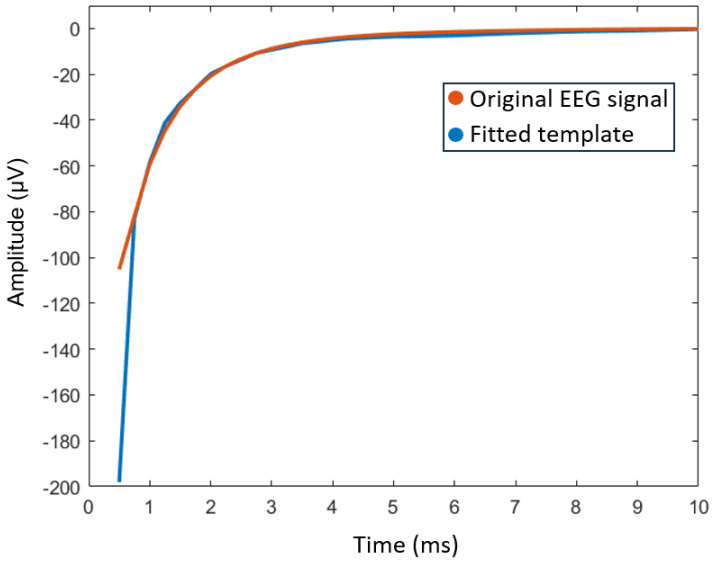

Figure 23: The fit of the template to the original EEG data is assessed for channel FP1, utilizing the relative error as a metric.

When performing template subtraction on the EEG signal, the resulting output is illustrated in Figure 24. Specifically, Figure 24a presents the outcomes of template subtraction for channel FP1, while Figure 24b extends the analysis to encompass all channels. Both figures initially exhibit a high-amplitude signal, attributed to a suboptimal fit at the beginning of the template. To rectify this issue, linear interpolation is applied, spanning from 0 to the mean amplitude of the previously processed signal. The ultimate output of template subtraction, combined with linear interpolation, is showcased in Figure 25. Notably, a period of high-frequency noise is observed until t=4ms, succeeded by a distinct and clear signal. The topography at t=6ms is notably smooth.

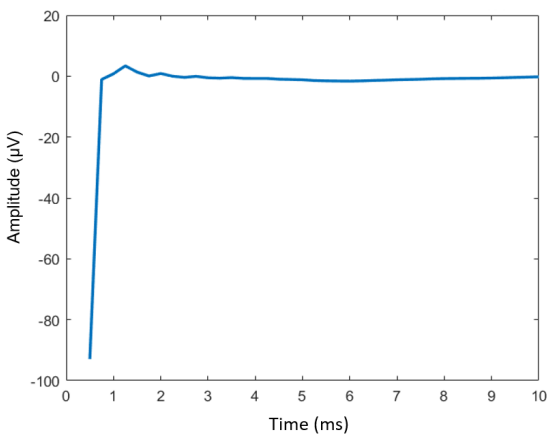

(a) Result of template subtraction of FP1.

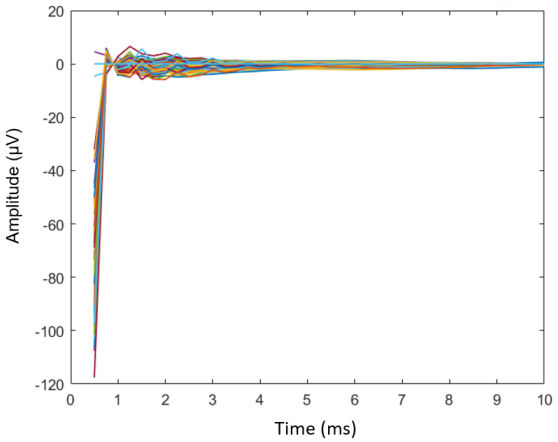

(b) Result of template subtraction of all channels.

Figure 24: Results of template subtraction. It shows a notably high amplitude signal at the onset, caused by a suboptimal fit at the beginning of the template.

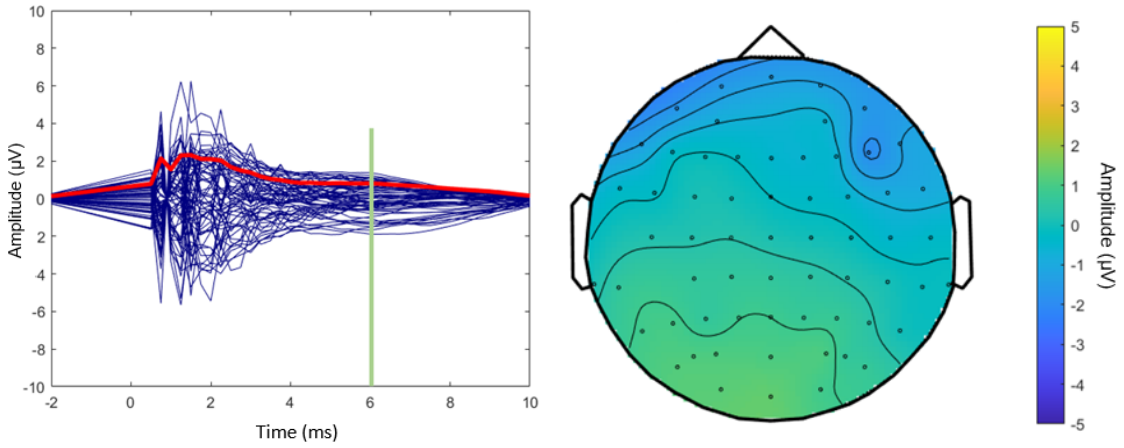

(a) Time series after filtering

(b) Spatial distribution after filtering

Figure 25: Results of template subtraction and linear interpolation. It reveals a presence of high-frequency noise until t=4ms, succeeded by a clear signal. The topography at t=6ms is distinctly clear.